JCB Journal of Cell Biology

ARTICLE

Dynamics of sister chromatid resolution during cell cycle progression

Rugile Stanyte[1], Johannes Nuebler[2], Claudia Blaukopf[1], Rudolf Hoefler[1], Roman Stocsits[3], Jan-Michael Peters[3], and Daniel W. Gerlich[1]

Faithful genome transmission in dividing cells requires that the two copies of each chromosome's DNA package into separate but physically linked sister chromatids. The linkage between sister chromatids is mediated by cohesin, yet where sister chromatids are linked and how they resolve during cell cycle progression has remained unclear. In this study, we investigated sister chromatid organization in live human cells using dCas9-mEGFP labeling of endogenous genomic loci. We detected substantial sister locus separation during G2 phase irrespective of the proximity to cohesin enrichment sites. Almost all sister loci separated within a few hours after their respective replication and then rapidly equilibrated their average distances within dynamic chromatin polymers. Our findings explain why the topology of sister chromatid resolution in G2 largely reflects the DNA replication program. Furthermore, these data suggest that cohesin enrichment sites are not persistent cohesive sites in human cells. Rather, cohesion might occur at variable genomic positions within the cell population.

Introduction

To transmit the genetic information through generations, cells must duplicate each chromosome's DNA and package both copies into separate cytological bodies termed mitotic sister chromatids. In vertebrate cells, the replicated DNA of each chromosome initially colocalizes within the same nuclear territory (Bickmore and van Steensel, 2013; Nagasaka et al., 2016). Sister chromatids become visible as separate rod-shaped structures only when cells enter mitosis, around the time when the nuclear envelope disassembles (Giménez-Abián et al., 1995; Kireeva et al., 2004; Liang et al., 2015; Nagasaka et al., 2016). However, individual genomic sites labeled by FISH often appear as pairs of fluorescent foci after their replication many hours before cells enter mitosis (Selig et al., 1992; Volpi et al., 2001; Azuara et al., 2003; Mlynarczyk-Evans et al., 2006; Schmitz et al., 2007; Nishiyama et al., 2010). Hence, at least parts of replicated chromosomes move apart long before sister chromatids become visible as separate cytological bodies. How this is regulated in time and to what extent it is influenced by the genomic neighborhood is unclear.

Although sister chromatids resolve during mitosis, they remain physically linked to enable correct attachment to the mitotic spindle (Nasmyth and Haering, 2009). This is mediated by the cohesin protein complex (Guacci et al., 1997; Michaelis et al., 1997), which forms a tripartite ring to topologically link DNA of sister chromatids (Gruber et al., 2003; Haering et al., 2008). Cohesin's interaction with chromosomes is regulated throughout the cell cycle by various cofactors. Before DNA replication, cohesin binds to chromosomes with a short residence time (Gerlich et al., 2006; Ladurner et al., 2016; Hansen et al., 2017; Rhodes et al., 2017) whereby the protein wings apart-like protein homolog (WAPL) promotes dynamic turnover (Kueng et al., 2006). During S phase, a fraction of cohesin converts to a stably chromatin-bound state (Gerlich et al., 2006) by acetylation of the SMC3 subunit and binding of Sororin (Schmitz et al., 2007; Ladurner et al., 2016). Sororin stabilizes cohesin on chromatin by counteracting WAPL; this function is required to maintain sister chromatid cohesion from S phase until mitosis (Schmitz et al., 2007; Nishiyama et al., 2010; Ladurner et al., 2016).

Besides holding sister chromatids together, cohesin also organizes chromatin within sister chromatids. Chromatids contain domains with high contact probability termed topologically associated domains (TADs; Dixon et al., 2012; Nora et al., 2012). Cohesin enriches at the boundaries of TADs and is required for their formation (Rao et al., 2014, 2017; Zuin et al., 2014a; Schwarzer et al., 2016; Gassler et al., 2017; Wutz et al., 2017). It has been hypothesized that cohesin forms TADs by extruding chromatin loops whereby the boundaries are specified by the protein CTCF (Nasmyth, 2001; Sanborn et al., 2015; Fudenberg et al., 2016; Busslinger et al., 2017; Rao et al., 2017).

[1]Institute of Molecular Biotechnology of the Austrian Academy of Sciences, Vienna BioCenter, Vienna, Austria; [2]Institute for Medical Engineering and Science, Massachusetts Institute of Technology, Cambridge, MA; [3]Research Institute of Molecular Pathology, Vienna BioCenter, Vienna, Austria.

Correspondence to Daniel W. Gerlich: daniel.gerlich@imba.oeaw.ac.at.

Genomic sites enriched for cohesin might not only represent TAD boundaries but might also represent sites of preferential sister chromatid cohesion. In fission yeast, cohesin chromatin immunoprecipitation (ChIP) sequencing (ChIP-seq) peaks that colocalize with the cohesin-loading factor Mis4 (nipped-b-like protein [NIPBL] in humans) represent sites of persistent sister chromatid linkage (Bhardwaj et al., 2016). In human cells, however, there is very little overlap between cohesin ChIP-seq peaks and NIPBL (Kagey et al., 2010; Zuin et al., 2014b; Busslinger et al., 2017). Moreover, cohesin can laterally diffuse along DNA (Davidson et al., 2016; Stigler et al., 2016) and relocate to distant genomic regions (Lengronne et al., 2004; Busslinger et al., 2017). Therefore, a substantial fraction of cohesin might occupy variable genomic positions in different cells within a heterogeneous population, which would not be detectable by conventional ChIP. Currently available chromosome conformation capture techniques also cannot detect linkage sites between sister chromatids because of the identical DNA sequences of sister chromatids. Whether the human genome encodes distinct sites of enhanced sister chromatid cohesion and how these would relate to cohesin enrichment sites have remained unknown.

In addition to cohesion, other factors might influence the spatial pattern of sister chromatid resolution. In vertebrate cells, the degree of sister locus separation during G2 appears to be elevated at sites with high transcriptional activity (Azuara et al., 2003; Mlynarczyk-Evans et al., 2006) and at genomic regions that replicate early (Selig et al., 1992). However, only few genomic loci have been investigated, and whether cohesin enrichment sites in the genomic vicinity affect sister locus resolution has remained unclear. Moreover, these prior studies of sister locus separation relied on FISH, which might induce artifacts owing to harsh sample preparation procedures.

Progress in live-cell genome labeling methodology provides new opportunities to investigate the spatial distribution of sister chromatid linkage sites and to follow their resolution as cells progress from S phase to mitosis. In this study, we used CRISPR/Cas9 technology (Chen et al., 2013) to generate a collection of human cell lines with fluorescently labeled endogenous genomic loci and investigated the resolution of sister chromatids by live-cell microscopy. Our study reveals that sister chromatids resolve by a dynamic process that initiates long before mitotic entry.

Results

A human cell line collection with fluorescently labeled endogenous genomic loci

To systematically probe the topology of sister chromatids in living human cells, we used single guide RNA (sgRNA)/Cas9 technology to target a catalytically inactive Cas9-monomeric–enhanced green fluorescent fusion protein (dCas9-mEGFP) to unique genomic regions. This technology efficiently labels unique repeat regions in the genome of human cells without compromising cell viability and with minimal effects on DNA damage (Chen et al., 2013). We identified candidate genomic sites for fluorescent labeling by analyzing the human tandem repeat database (Gelfand et al., 2007) and mapping all genomic regions that contain at least 20 copies of a single sgRNA target site within 20 kb. We selected 113 regions and individually introduced their corresponding sgRNAs into HeLa cells expressing dCas9-mEGFP. Imaging of live cells by confocal microscopy revealed discrete nuclear foci for 47 of the 113 regions. We pursued 16 regions that reside on 11 different chromosomes, are at least 0.5 Mbp from centromeres/telomeres, and are located within various genomic contexts including protein-coding genes, long noncoding RNA genes, and intergenic regions (Table S1). To this end, we generated 16 HeLa cell lines that stably express a single sgRNA and doxycycline-inducible dCas9-mEGFP. After induction of dCas9-mEGFP, we imaged live cells by confocal microscopy and analyzed all cells expressing low to middle levels of dCas9-mEGFP (to avoid saturation of the signal by nucleoplasmic background fluorescence). For each cell line, we detected a small number of fluorescent foci in the nucleus of >90% of the analyzed cells whereby the number of foci per nucleus matched the corresponding number of sgRNA target alleles in HeLa cells (Fig. S1; Landry et al., 2013). The mean fluorescence of different alleles within individual nuclei varied to some extent, which might be caused by their different z position relative to the focal sectioning planes, or which might reflect allele-specific copy number variations of the sgRNA target sequence. Overall, the high locus-labeling efficiency in our collection of 16 cell lines enabled us to assess the topology of sister chromatids in distinct genomic contexts.

Labeling of genomic sites with dCas9-mEGFP/sgRNA might perturb cell-essential processes such as DNA replication. To test this, we investigated cell proliferation, mitotic duration, and nuclear morphology. We performed long-term time-lapse microscopy of eight randomly selected cell lines with dCas9-mEGFP/sgRNA–labeled loci and found that their nuclear morphology and proliferation rates were indistinguishable from control cells and that they progressed through mitosis without delay (Fig. S2, A–F). Hence, dCas9-mEGFP/sgRNA labeling does not impair essential cell functions.

Monitoring sister chromatid resolution in live cells

To study the organization of sister chromatids in each cell line, we collected mitotic cells by mechanical shakeoff, seeded them into chambered coverslips, and imaged them by 3D confocal time-lapse microscopy throughout an entire cell cycle (Fig. 1, A and B). For each cell, we monitored entry into the next mitosis based on cell rounding and the release of the nucleoplasmic pool of dCas9-mEGFP into the cytoplasm (Fig. 1 B). We selected image frames from 0.6–2.4 h preceding mitosis, which corresponds with G2 phase in HeLa cells (Held et al., 2010), for further analysis.

In G2 nuclei, the fluorescently labeled genomic sites appeared either as a single dot ("singlet") or as a pair of dots ("doublet;" Fig. 1, C–E). Singlets represent unreplicated genomic loci or replicated loci where sister DNA strands are at a distance below the resolution limit. Doublets represent replicated sister loci that are spaced apart beyond the resolution limit. To determine the center positions of fluorescent dots, we extracted image subregions around each singlet or doublet for automated analysis. Owing to the low z sampling rate, which could not be increased because of phototoxicity limitations, we could not accurately measure distances in 3D space. We therefore performed all distance measurements in 2D optical sections that contained the brightest

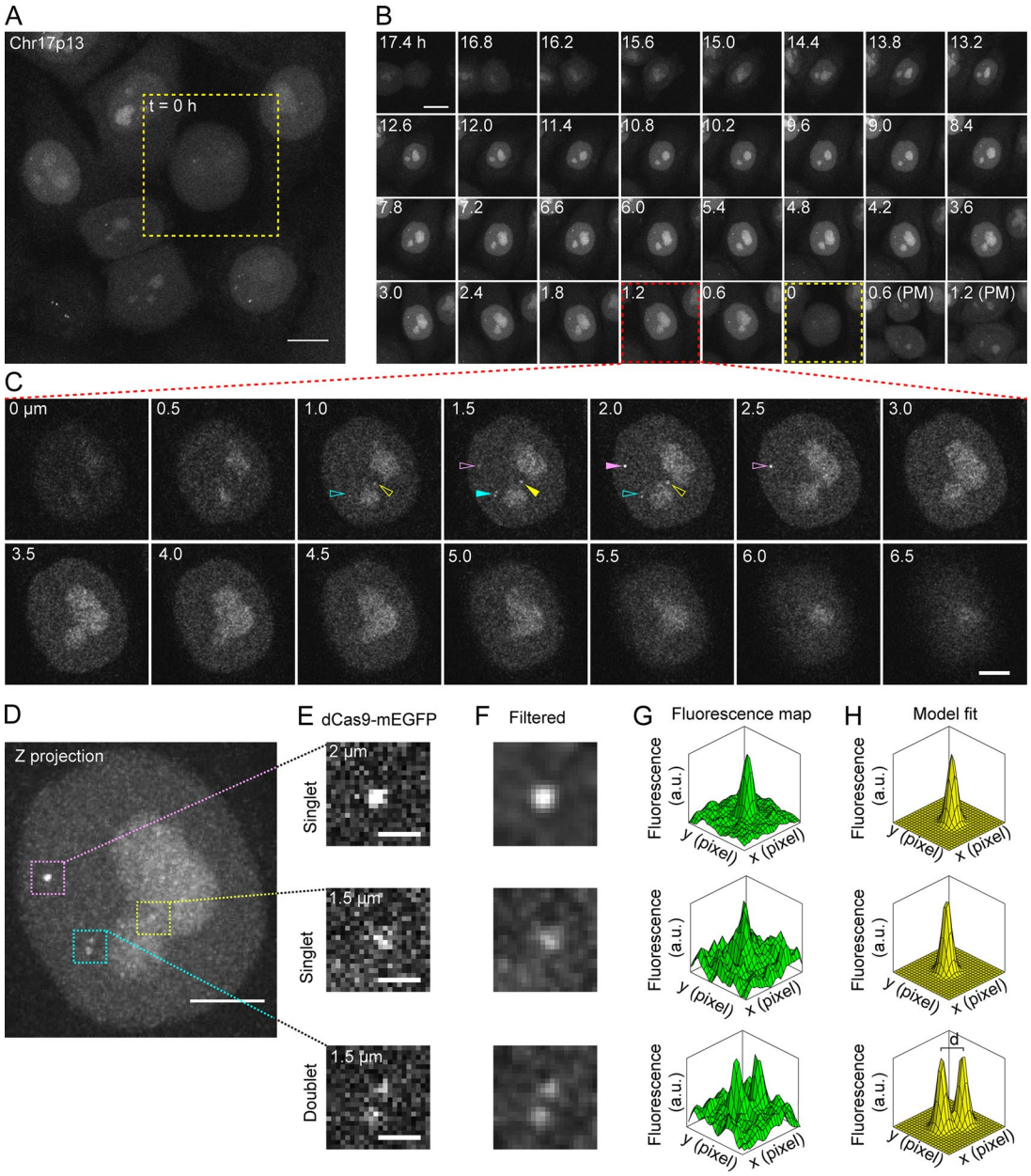

Figure 1. **3D live-cell imaging of endogenous genomic loci throughout the cell cycle. (A–D)** Confocal live-cell microscopy of HeLa cells expressing dCas9-mEGFP and sgRNA targeting Chr17p13 over 24 h with a time lapse of 36 min and 21 z sections at 0.5-µm spacing. **(A)** Maximum-intensity projection at 17.4 h after imaging onset (yellow square indicates mitotic cell). **(B)** Time-lapse of maximum-intensity projections for cell shown in A. 0 h, mitosis; PM, postmitosis. Red box indicates time point shown in C. **(C)** Individual z sections at 1.2 h before mitosis. Arrowheads indicate all optical sections with three fluorescently labeled genomic loci, and the filled arrowheads indicate the optical section with highest fluorescence signal. **(D–H)** Image analysis procedure. **(D)** 3D maximum-intensity z projection of cell shown in C. Boxes indicate regions containing labeled alleles. **(E)** Single z section containing brightest dCas9-mEGFP signal for the respective alleles. Bars: (A and B) 10 µm; (C and D) 5 µm; (E) 1 µm. **(F)** Gaussian filtering of E. **(G)** Fluorescence density distribution of F. **(H)** Gaussian mixture model fitted to G. d indicates distance between the means of two Gaussian functions.

fluorescent signal for the respective labeled allele (Fig. 1 C, filled arrowheads; and Fig. 1, D and E). We reduced image noise by filtering and then fitted a mixture model of two Gaussian functions to the image subregions using an automated optimization algorithm (Fig. 1, F–H; see Materials and methods for details) to obtain the coordinates of two fluorescent point sources in singlets as well as in doublets.

To estimate the accuracy of the image analysis method, we computationally simulated images based on a pair of fluorescence point sources, the microscope's point spread function, and detector noise (Fig. S2, G–L). We then determined the distance between simulated fluorescent point sources by fitting the Gaussian mixture model. For simulations with distances >300 nm, the measurements matched ground truth with an accuracy of 12.4 ± 14.5 nm (mean ± SD), but the model fitting did not yield accurate results at smaller distances (Fig. S2, G–L). We hence classified fluorescent dots as doublets when the measured distance was >300 nm or singlets when the measured distance was ≤300 nm.

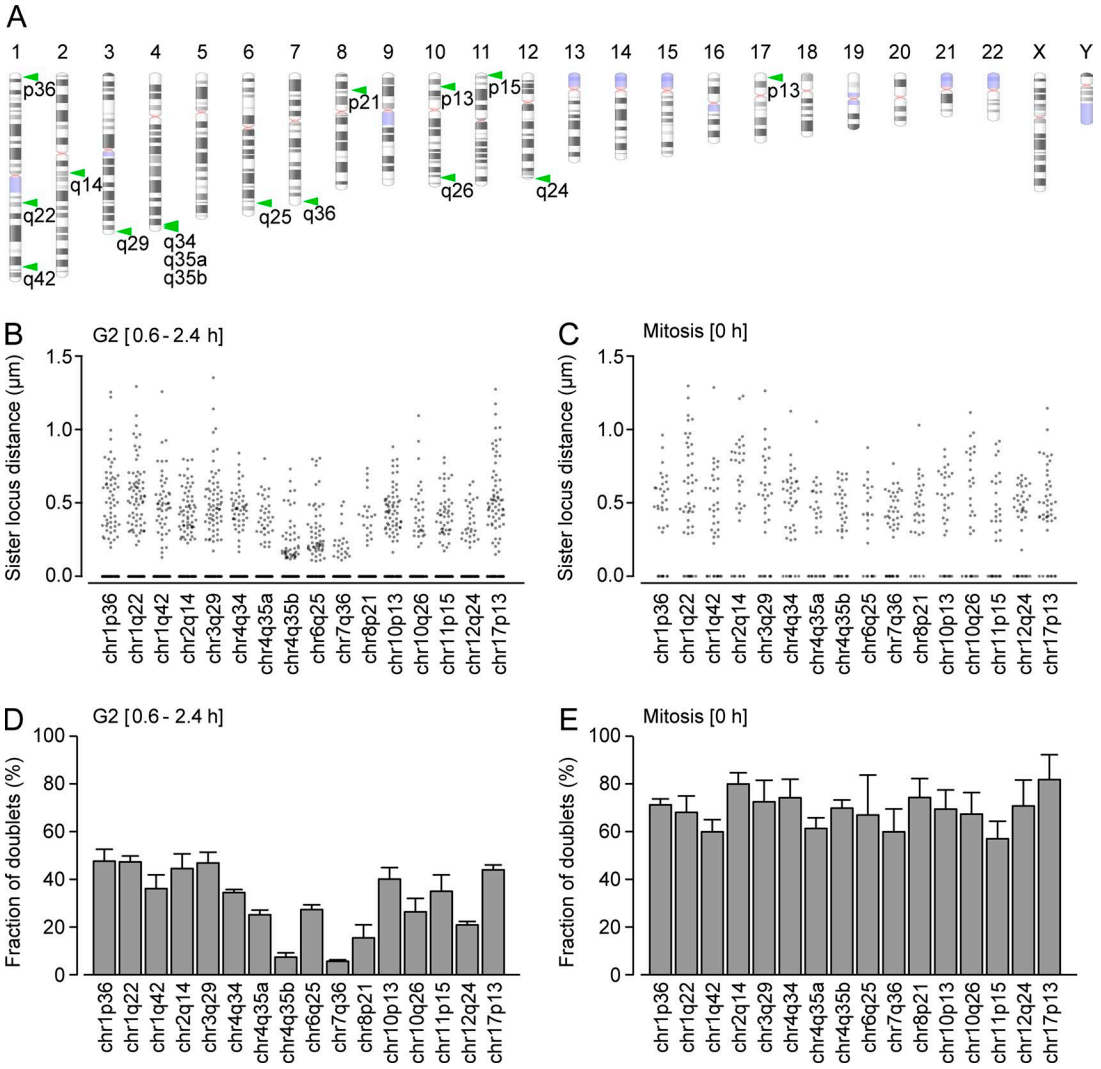

Figure 2. **Mapping sister chromatid resolution in live human cells. (A)** Position of dCas9-mEGFP/sgRNA–labeled genomic sites (green arrowheads) contained in the HeLa cell line collection on human chromosome ideogram (Schneider et al., 2017). Annotations indicate chromosome and band numbers. Blue indicates unmapped chromosome regions, and pink indicates centromeres. See Table S1 for details. **(B–E)** Quantification of sister locus separation in 16 cell lines as in A based on live-cell microscopy and image analysis as in Fig. 1. **(B)** Sister locus distance in G2 (0.6–2.4 h preceding mitosis). Each dot indicates distance measurement from one allele; n = 120 randomly subsampled distance measurements for each cell line based on three independent experiments. **(C)** Sister locus distance as in B during mitosis. $n \geq 23$ measurements. **(D)** Fraction of doublets (spots with distance >300 nm) in G2 based on data shown in B. Significant differences between genomic sites ($P < 10^{-7}$ by one way ANOVA). **(E)** Fraction of doublets in mitosis was calculated for the data shown in C. The fraction of doublets is not significantly different at different genomic positions ($P = 0.75$ by one-way ANOVA). Error bars indicate means ± SEM. n = 3 experiments.

This approach provides an objective, consistent, and accurate means to determine the degree of sister locus separation.

To investigate the organization of sister chromatids during G2, we asked whether sister loci maintain a persistent linkage at any of the labeled genomic sites in our cell line collection. We imaged each of the 16 cell lines as described above. For all 16 genomic sites, we found that a fraction of loci appears as doublets during G2, with sister loci spaced up to ∼1.5 µm apart (Fig. 2, A and B). The distance between sister loci during interphase was often as large as in mitotic chromosomes (Fig. 2 C). Hence, none of the investigated genomic sites displayed constitutive sister locus linkage.

To investigate whether sister locus separation depends on the genomic context, we calculated the fraction of doublets in G2. This revealed significant differences between genomic sites ($P < 10^{-7}$ by one-way ANOVA test) ranging from 5.7% to 47.8% doublets (Fig. 2 D). During mitosis, the fraction of doublets was higher, ranging from 57.2% to 82.0% (Fig. 2 E), and it did not differ significantly between different genomic sites ($P = 0.75$ by one-way ANOVA test). These data suggest that the spatial organization of sister chromatids during G2 depends on local genomic features.

To investigate potential perturbations caused by the in vivo labeling method, we used FISH to visualize six sgRNA target sites in WT HeLa cells as well as in cells expressing dCas9-mEGFP and the respective sgRNA. We synchronized cells to G2 by a release from double-thymidine block and performed FISH, which revealed a high correlation of sister locus separation between WT and labeled cells (Fig. 3, A–D; Pearson correlation coefficient, $R^2 = 0.81$). Thus, the dCas9-mEGFP/sgRNA labeling and FISH data support our inference that the topology of sister chromatid separation in interphase depends on the genomic context.

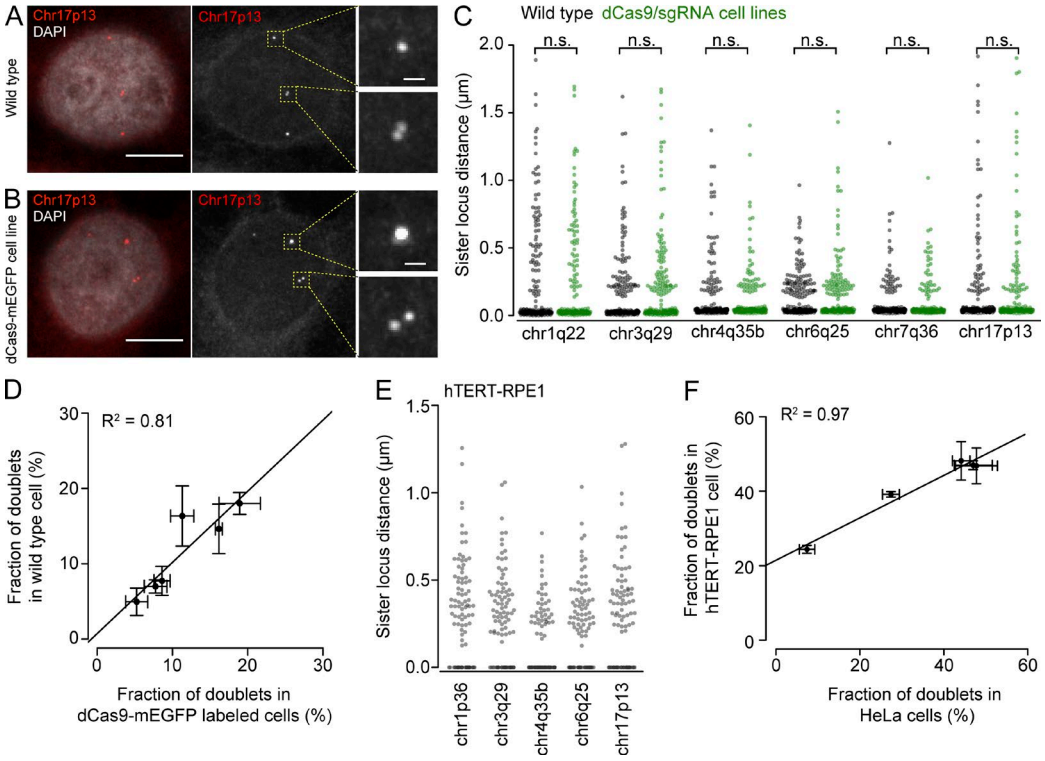

Figure 3. **Mapping sister chromatid resolution by FISH and in hTERT-RPE1 cells. (A and B)** Comparison of WT HeLa cells and HeLa cells expressing dCas9-mEGFP and sgRNA targeting Chr17p13. Cells were synchronized to G2 by release from double-thymidine block and stained with FISH probes targeting Chr17p13. Yellow boxes indicate labeled alleles as shown in insets. DNA was stained with DAPI. Bars: (main images) 10 µm; (insets) 1 µm. **(C)** Quantification of sister locus distances based on FISH staining as in A and B for six genomic sites in WT cells and in cell lines expressing dCas9-mEGFP together with the sgRNA targeting to the corresponding locus. *n* = 230 loci from three independent experiments for each genomic site. n.s., P > 0.05; nonparametric Wilcoxon rank test. **(D)** Fraction of doublets based on data shown in C. **(E)** Sister locus distances in five dCas9-mEGFP/sgRNA–labeled hTET-RPE1 cell lines determined by live-cell microscopy as in Fig. 1. *n* = 100 randomly subsampled distance measurements for each cell line. **(F)** Fraction of doublets in G2 (0.6–2.4 h before mitosis) in hTERT-RPE1 cells based on E compared with the fraction of doublets in HeLa Kyoto cells (as in Fig. 2 D). Dots and error bars indicate means ± SEM. *n* ≥ 3 experiments.

Finally, we asked whether the locus-specific variation of sister chromatid separation is conserved between different cell types. We generated noncancer retinal pigmented epithelial (hTERT-RPE1) cell lines expressing dCas9-mEGFP and sgRNA targeting five different loci (Chr1p36, Chr3q29, Chr4q35b, Chr6q25, and Chr17p13, respectively) and imaged them by 3D live-cell confocal microscopy. The extent of sister locus separation in G2 for each chromosomal site was highly correlated between HeLa and hTERT-RPE1 cells (Fig. 3, E and F; Pearson correlation coefficient, R^2 = 0.97). Thus, the genome specifies the sister chromatid resolution topology in a cell type–independent manner.

Proximity to cohesin ChIP-seq peaks does not suppress sister locus separation

The degree of sister locus separation might be governed by the distance to genomic cohesin enrichment sites. To investigate this, we calculated the genomic distance between the center point of each dCas9-mEGFP/sgRNA–labeled locus and the nearest cohesin enrichment site based on ChIP-seq profiles of the SMC3 subunit in G2 HeLa cells (Fig. 4 A; Ladurner et al., 2016). We then compared this to the degree of sister locus splitting in G2 based on the live-cell imaging data shown in Fig. 2 D. Unexpectedly, increased distance from SMC3 ChIP-seq peaks did not correlate with an elevated doublet frequency (Fig. 4 B). Instead, loci in genomic proximity to SMC3 ChIP-seq peaks appeared as doublets more frequently than those further away (Pearson correlation coefficient, R^2 = 0.36) even when very close (the smallest genomic distance of 2.2 kb corresponding with a Euclidian distance of 140 nm for a fully extended 10-nm chromatin fiber). Hence, sister loci can resolve substantially even when close to genomic cohesin enrichment sites.

We next considered that only a subset of cohesin enrichment sites might contribute to sister chromatid cohesion. Specifically, we asked whether only SMC3 enrichment sites that also contain the cohesin stabilization factor Sororin influence the degree of sister locus splitting. We calculated the genomic distance between dCas9-mEGFP/sgRNA–labeled loci and the nearest SMC3 ChIP-seq peak that also contained Sororin in G2 (Fig. 4 C; Ladurner et al., 2016). This showed that genomic proximity to Sororin/SMC3 ChIP-seq peaks also did not correlate with a reduced fraction of doublets (Fig. 4 D). Together, these data suggest that cohesin and Sororin ChIP-seq peaks do not represent sites of preferential sister chromatid cohesion, at least at the scale that can be probed by our cell line collection.

Degree of sister locus separation correlates with nuclear positioning, chromatin state, and DNA replication timing

We next searched for other genomic features that might explain the variations of sister locus separation. To detect potential

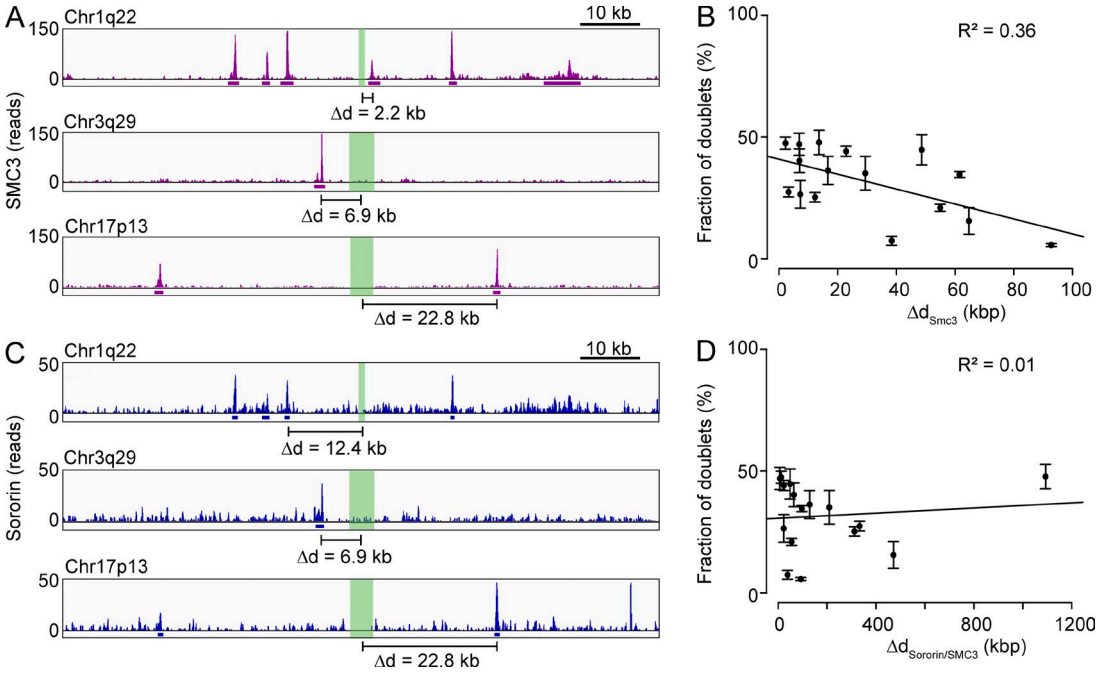

Figure 4. **Genomic regions close to cohesin/Sororin ChIP-seq peaks frequently separate sister loci during G2. (A)** Genomic maps of SMC3 binding profiles around three dCas9-mEGFP/sgRNA–labeled loci. Magenta indicates DNA sequencing read counts and annotated peaks for SMC3 ChIP-seq data from Ladurner et al. (2016). Green indicates sgRNA target regions used for dCas9-mEGFP imaging. Genomic distances were calculated between the center of each sgRNA target region and the nearest SMC3 ChIP-seq peak. **(B)** Genomic distances between sgRNA target regions and the nearest SMC3 ChIP-seq peak for all 16 genomic sites labeled by dCas9-mEGFP/sgRNA (Table S1); related to the fraction of doublets in G2 as shown in Fig. 2 D. **(C)** Genomic maps of Sororin-binding profiles around the loci shown in A. Blue indicates DNA sequencing read counts and annotated peaks for Sororin ChIP-seq data from Ladurner et al. (2016). Green indicates target regions of sgRNAs used for dCas9-mEGFP imaging. Genomic distances were calculated between the center of each sgRNA target region and the nearest Sororin ChIP-seq peak that also contained SMC3. **(D)** Genomic distances between sgRNA target regions and the nearest genomic site containing ChIP-seq peaks of SMC3 and Sororin; related to the fraction of doublets in G2 as shown in Fig. 2 D. Bars show means ± SEM. *n* = 3 experiments.

implications of the chromatin state, we tested whether the degree of sister locus splitting correlates with nuclear positioning, as transcriptionally inactive constitutive heterochromatin localizes to the nuclear periphery, whereas actively transcribed euchromatin predominantly localizes to interior regions of the nucleus (Pueschel et al., 2016). We determined the distances of labeled loci from the nuclear boundary for each of the 16 cell lines (Fig. 5, A–C) and correlated this with the sister locus splitting data (see Fig. 2 D). This showed that genomic sites closely associated with the nuclear periphery generally had a low fraction of doublets in G2 (Fig. 5 D).

To further test whether sister locus separation correlates with nuclear localization, we considered DNA sequencing–based annotations of genomic regions associated with the nuclear periphery termed lamina-associated domains (LADs; Guelen et al., 2008). Of the 16 genomic sites contained in our cell line collection, five reside in LADs (Table S1). These genomic sites indeed localized significantly closer to the nuclear rim in our imaging experiments compared with genomic sites residing outside of LADs (Fig. 5 E). The fluorescently labeled loci residing in LADs had a significantly smaller fraction of doublets in G2 compared with loci residing outside of LADs (Fig. 5 F). Thus, genomic regions associated with the nuclear periphery separate sister loci less frequently than genomic regions residing predominantly in the nuclear interior.

To investigate whether the degree of sister locus separation correlates with chromatin states, we considered HeLa ChIP-seq data of histone modifications (ENCODE Project Consortium, 2012). We determined whether the 100-kb regions centered around each genomic target site contained marks of transcriptionally active euchromatin (H3K9 acetylation, H3K27 acetylation, and H3K4 trimethylation) or marks of transcriptionally repressed heterochromatin (H3K9 trimethylation and H3K27 trimethylation). We consistently observed that labeled loci that had active euchromatin marks in their vicinity split more frequently, whereas labeled loci that had repressive heterochromatin marks in their vicinity split less frequently (Fig. 5, G–K). For the individual histone modifications, these differences were not statistically significant (by unpaired two-sided *t* tests at $\alpha = 0.05$) except for H2K9 acetylation, but considering multiple modifications to classify euchromatin (only active marks) or heterochromatin (only repressive marks), we did detect significant differences (Fig. 5 L; $P = 0.02$ by unpaired two-sided *t* tests). Thus, genomic loci residing in euchromatic regions have a higher probability to separate their sisters than those residing in heterochromatin.

We next investigated whether the degree of sister locus separation correlates with transcriptional activity. We considered mRNA expression–profiling data from HeLa cells (ENCODE Project Consortium, 2012) and found that sister loci residing in the vicinity of transcribed chromatin were split more frequently than sister loci residing in untranscribed regions ($P = 0.003$ by unpaired two-sided *t* tests; Fig. 5 M). Hence, open chromatin

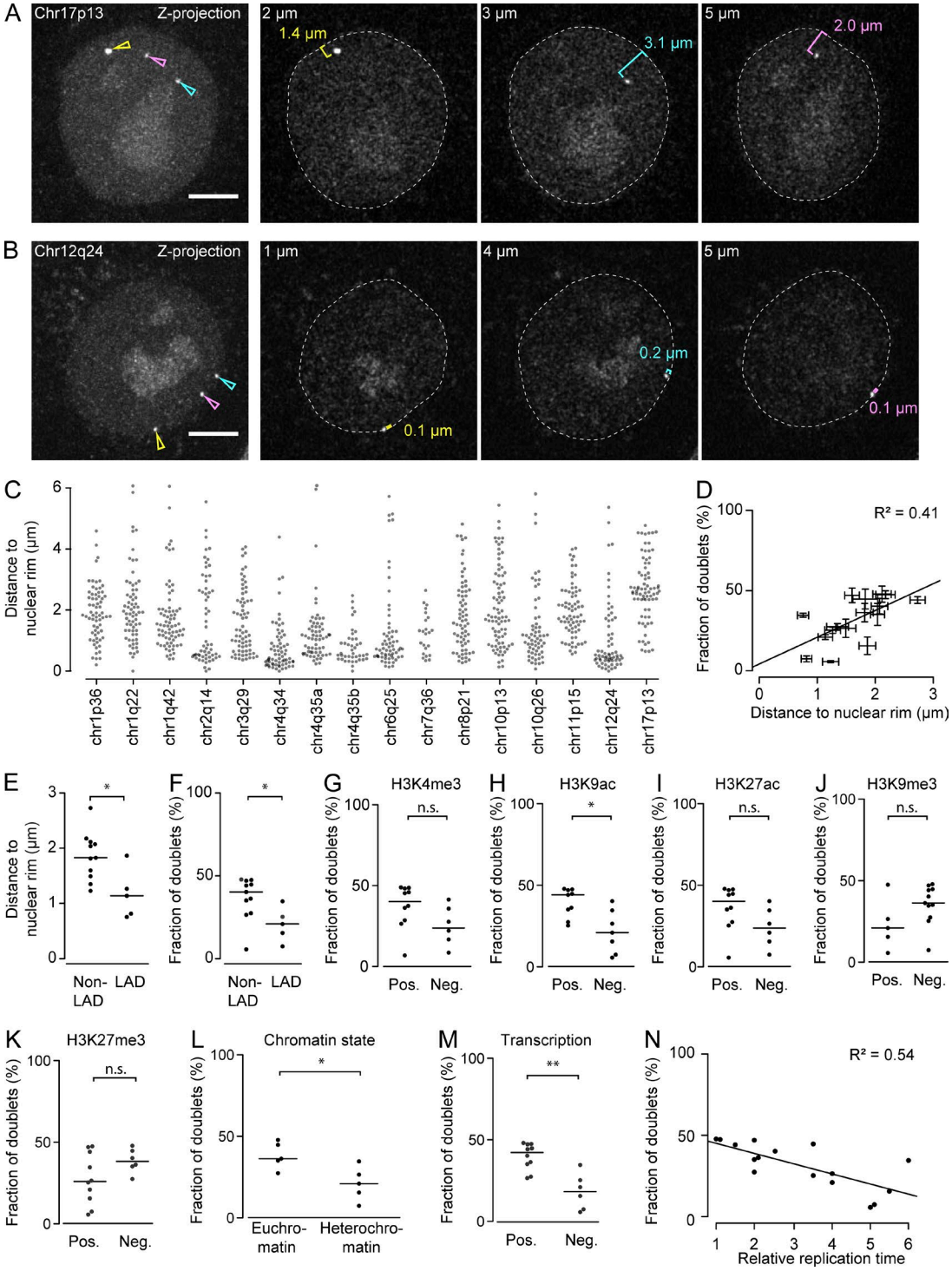

Figure 5. **Degree of sister locus separation correlates with nuclear position, chromatin state, and replication timing. (A–D)** Nuclear positioning of dCas9-mEGFP–labeled loci. **(A)** Z projection and individual *z* sections from live cell expressing dCas9-mEGFP and sgRNA targeting Chr17p13. The nuclear rim (dashed line) was determined based on the nucleoplasmic background fluorescence, and the distance to dCas9-mEGFP–labeled loci was measured in individual *z* sections. **(B)** As A but for Chr12q24 locus. Arrowheads indicate three labelled alleles in maximum-intensity *z* projection images. Bars, 5 µm. **(C)** Distance to the nuclear rim for 16 genomic loci (Table S1) as in A and B. Differences between genomic positions are significant ($P < 10^{-16}$ by Kruskal-Wallis rank sum test; $n \geq 23$ measurements per locus). **(D)** Relationship between locus distance to the nuclear rim and the fraction of doublets during G2 (as in Fig. 2 D). Error bars indicate means ± SEM. $n = 3$ experiments for fraction of doublets; $n \geq 23$ nuclear rim distance measurements. **(E and F)** The 16 labeled loci were classified according to their position within or outside of LADs (Guelen et al., 2008), and the respective mean distance to the nuclear rim (E) or fraction of doublets (F) were plotted for each locus. *, $P = 0.02$ by unpaired two-sided *t* test. **(G–L)** Correlation between sister locus separation and histone modifications in 100-kb regions centered around labeled loci based on HeLa data from ENCODE Project Consortium (2012). Pos. indicates the presence of at least one of the respective chromatin marks, and Neg. indicates absence. Dots indicate labeled loci. **(G–I)** Transcriptionally active chromatin marks in H3K4me3 (G), H3K9ac (H), and H3K27ac (I). **(J and K)** Repressed chromatin marks in H3K9me3 (J) and H3K27me3 (K). n.s., $P > 0.05$; *, $P = 0.01$; unpaired two-sided *t* test. **(L)** Classification

and transcriptional activity correlate with increased sister locus separation in G2.

Heterochromatin at the nuclear periphery replicates late during S phase compared with euchromatin of the nuclear interior (Leonhardt et al., 2000). The high incidence of sister locus splitting at genomic sites that preferentially localize to the nuclear interior might hence result from early DNA replication. To investigate this, we related our sister locus separation measurements to published DNA replication timing data from HeLa cells (Hansen et al., 2010; ENCODE Project Consortium, 2012). Our live-cell imaging data of G2 cells (Fig. 2 D) showed that dCas9-mEGFP–labeled loci residing in early replicating genomic regions appeared as doublets more often than those residing in late-replicating regions (Fig. 5 N). Thus, the spatial organization of sister chromatids correlates with the DNA replication program.

Dynamics of sister chromatid resolution

We next investigated the dynamics of sister locus separation during cell cycle progression. First, we aimed to determine when sister loci start to split. We followed the trajectories of individual labeled alleles from G1 until mitotic entry using the data shown in Fig. 1. For the early replicating locus Chr17p13, the first doublets appeared >12 h before mitotic entry (Fig. 6, A–D). By 8 h before mitotic entry, doublets had appeared in >50% of the trajectories, and by 2 h before mitotic entry, they appeared in 93% of the trajectories (Fig. 6, C and D; n = 40 trajectories from 27 cells). Thus, sister chromatids at this genomic site can split many hours before cells enter mitosis. Moreover, the time point of initial sister locus separation varies several hours between different alleles and cells.

After the initial split, sister loci might remain separate until cells enter mitosis. However, analysis of individual allele trajectories showed that doublets frequently alternate with singlets before cells enter mitosis (97% of the trajectories for Chr17p13; n = 37; see Fig. 6 C). The alternation between singlets and doublets, however, does not imply that sister loci switch between linked and dissociated states, as our imaging setup resolves fluorescent dots only above distances above ∼300 nm along the x–y image plane. Furthermore, singlets might represent sister loci that separate even further apart along the z axis, which we cannot reliably quantify owing to the low optical sectioning along the z axis. Nevertheless, these data show that replicated interphase chromosomes form a dynamic structure in which sister loci continuously move.

Although the cell population progressed toward G2, the incidence of doublets gradually increased to ∼50%, and upon mitotic entry, it increased to ∼80% within a single time frame of 36 min (Fig. 6, C and D). This is still below the cumulative frequency of first split measured in single-allele trajectories at late-interphase stages, consistent with dynamic alternations between singlets and doublets. The gradual increase of doublets during interphase progression might be explained by the variable onset of sister locus splitting in different cells or alleles or by a continuous and slow drift separating sister loci. To investigate this, we realigned all trajectories to the time of first doublet appearance. We found that after the initial split, the incidence of doublets did not increase further (Fig. 6 E). This is consistent with a single rapid process releasing sister loci into separated sister chromatids.

To investigate whether sister loci continue to move further apart once they have been released, we analyzed distances between separated sister loci in doublets at different periods of interphase. Although the fraction of doublets increased as cells progressed toward G2, the mean distances between sister loci in doublets barely changed (Fig. 6, F and G). This is consistent with a model where sister loci separate by a single event and then rapidly equilibrate their distances within dynamic sister chromatids.

To further investigate this, we tested whether the sister locus separation measurements fit to a mathematical model of dynamic equilibrium polymers linked by cohesin complexes (see Materials and methods for details). The dynamic equilibrium model predicts that the distribution of relative sister locus positions in 3D nuclear space follows a 3D Gaussian function. In 2D image projections as in our experimental microscopy data, the distribution of sister locus distances according to this model thus follows a Rayleigh distribution $p(d) = d/s^2\ exp(-d^2/2s^2)$, where d is the 2D sister locus distance, and the only parameter s determines the scale of the distribution. We fitted Rayleigh functions to the distance distributions of doublets at different cell cycle stages and obtained very good agreement (Fig. 6 F, red lines). The observed sister locus distances are hence consistent with a model whereby sister loci rapidly equilibrate their relative positions after the initial split.

A dynamic equilibrium model relies on the assumption that sister loci explore their equilibrium distances quickly after replication. To assess this, we considered the diffusional mobility of individual genomic loci. To improve signal-to-noise for high time-resolution imaging experiments, we generated a HeLa cell line expressing dCas9 tagged with the SunTag system (Tanenbaum et al., 2014). We individually introduced sgRNAs targeting Chr17p13, Chr1q22, Chr3q29, or Chr6q25 to generate four different cell lines, which yielded approximately fourfold brighter dots compared with the respective dCas9-mEGFP–labeled loci (example shown in Fig. S2, M–O). We synchronized cells to S phase by collecting mitotic cells and growing them for 12 h and then recorded confocal microscopy videos at two frames per second. We automatically tracked sister loci and identified trajectory runs containing doublets for at least 10 s length to compute root mean square displacements (RMSDs) for individual sister loci (Fig. 6, H and I). RMSDs increased with time as a power law RMSD = A $t^{1/2}$ with

of chromatin state surrounding the labeled loci based on the presence of only active chromatin marks (H3K4me3, H3K9ac, and H3K27ac) or only repressive marks (H3K9me3 and H3K27me3) as shown in G–K. *, P = 0.02; unpaired two-sided t test. **(M)** Transcriptional activity in the 100-kb region centered around labeled loci based on polyadenylated RNA transcript profiling in HeLa cells (ENCODE Project Consortium, 2012). **, P = 0.003; unpaired two-sided t test. **(E–M)** Bars indicate medians. **(N)** Relationship between sister locus splitting during G2 and DNA replication timing (based on Hansen et al. [2010], whereby class 1 is earliest and class 6 is latest) for 16 labeled loci.

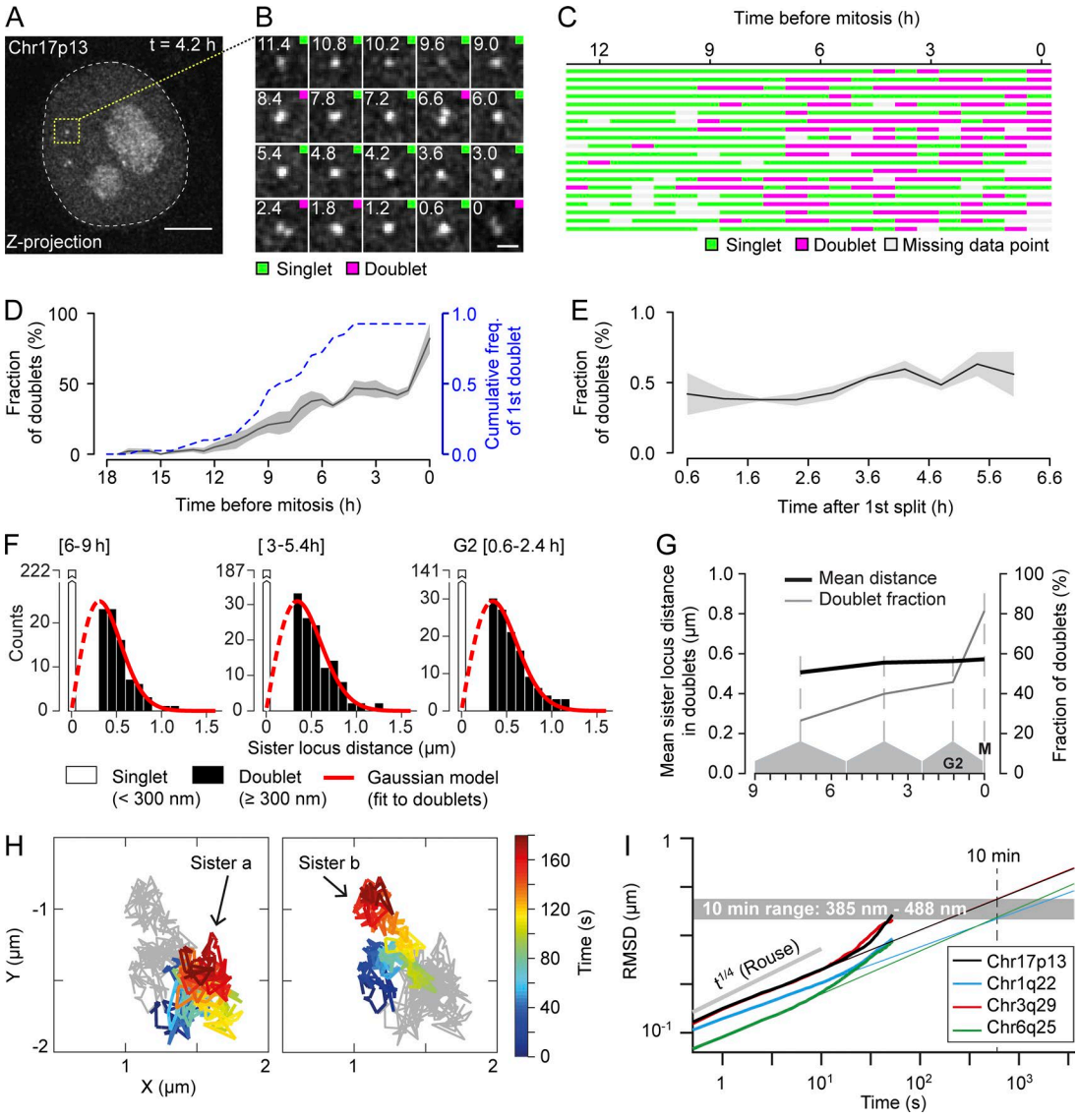

Figure 6. **Dynamics of sister locus resolution from S phase until mitosis for Chr17p13. (A–G)** Analysis of individual locus trajectories from imaging data as shown in Figs. 1 and 2. **(A and B)** Cell expressing dCas9-mEGFP and sgRNA targeting locus Chr17q13 (A). The dashed white line indicates nuclear rim, and the yellow box indicates region for trajectory analysis shown in B. Time points are relative to mitosis (t = 0 h). Colored squares indicate doublet (magenta) or singlet (green), respectively, based on automated analysis as in Fig. 1 (D–H). Bars: (A) 5 µm; (B) 1 µm. **(C)** 20 trajectories of individual alleles for Chr17q13 as shown in B. **(D)** Fraction of doublets based on trajectories as in C. n = 3 experiments. The dashed line shows cumulative frequency of first doublet detected in individual trajectories. n = 40 trajectories. **(E)** Fraction of doublets as in D after aligning all the trajectories to the first observed doublet. Solid lines and shaded areas indicate means ± SEM. **(F)** Distribution of sister locus distances for data shown in A–E at indicated cell cycle periods and Rayleigh distributions (corresponding with a Gaussian model) fit to the doublet distance distributions. **(G)** Mean distance between sister loci in doublets based on data shown in F. **(H and I)** Diffusional mobility of dCas9-SunTag–labeled genomic sites. Cells synchronized to S/G2 were imaged with a time lapse of 0.5 s, and doublets were considered for diffusional mobility analysis. **(H)** Representative trajectories for Chr17p13. Colored trajectories indicate one of the sister loci; the gray trajectory indicates the respective other sister. **(I)** RMSD analysis for Chr17p13 and three other genomic sites. n > 51 individual allele trajectories. Thick lines indicate measured data, and thin lines indicate extrapolations based on the initial curve segments up to 10 s. The gray line indicates mobility of a Rouse polymer model.

an exponent α/2 of ∼0.2 and A ∼0.13 µm/s$^{1/2}$, consistent with previous observations in B lymphocytes (Lucas et al., 2014). To estimate the space explored by loci within 10 min, we extrapolated the power law determined at 0.5–10 s and found RMSDs ranging between 390 and 490 nm for the different genomic loci, comparable with the mean sister distances in doublets. Collectively, these data are consistent with a dynamic chromatin model where after initial separation, sister loci quickly equilibrate their relative positions.

We next investigated the dynamics of sister chromatid resolution at other genomic positions. We first studied nine additional cell lines with fluorescently labeled loci that replicate in the first half of S phase. For all of these loci, we observed a substantial fraction of doublets 9–12 h before mitotic entry and multiple alternations between singlets and doublets in individual allele trajectories (Fig. 7, A and B; and Fig. S3, A–I). The distance between sister loci in doublets did not increase during interphase progression (Fig. 7 C), and the fraction of doublets did not increase after the

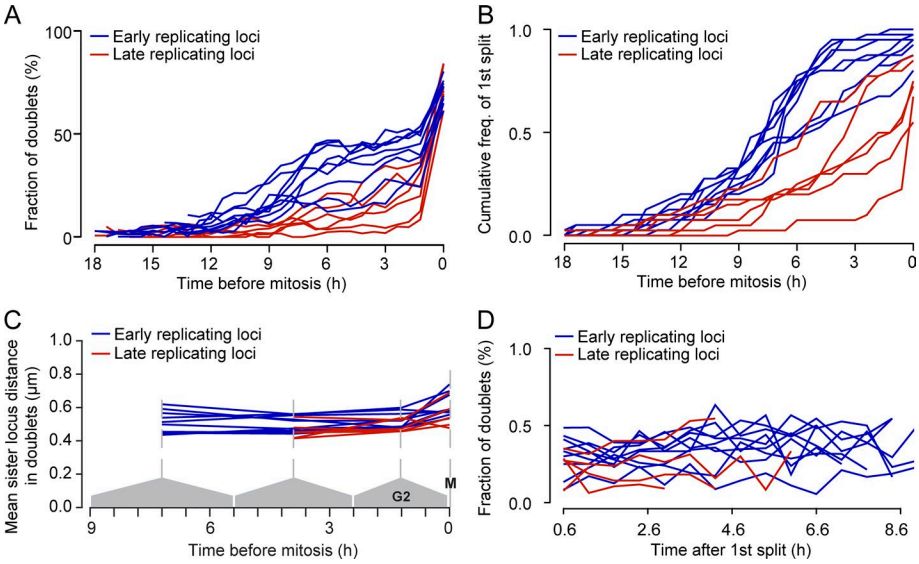

Figure 7. **Dynamics of sister locus resolution from S phase until mitosis for 15 genomic sites. (A)** Fraction of doublets as in Fig. 6 D for nine early replicating (blue) and six late-replicating (red) loci. Full data are in Fig. S3 (A–I). **(B)** Cumulative frequency of first split event for data shown in A; see Fig. S3 (J–O). **(C)** Mean distance between sister loci in doublets calculated as in Fig. 6 G. **(D)** Fraction of doublets in trajectories aligned to the first doublet for loci shown in A.

initial split for any of the genomic sites (Fig. 7 D). Overall, these data indicate that sister loci at various early replicating genome regions resolve with similar kinetics, albeit to a variable extent.

We investigated six cell lines with labeled genomic sites residing in late-replicating chromosome regions and found that the doublet fraction for these loci increased substantially later than observed in early replicating loci (Figs. 7 A and S3, J–O). However, at 2.4 h before mitosis, most of the individual trajectories had shown at least one doublet for any of the labeled genomic sites (Figs. 7 B and S3, J–O), confirming that DNA replication was largely complete (with the exception of Chr7q36; see Fig. S3 L). Late-replicating loci did not move further apart, and the probability of separation did not increase after their initial split (Fig. 7, C and D). Hence, all investigated genomic sites show consistent patterns of sister chromatid resolution kinetics.

Sororin delays sister locus separation during interphase

Our observations suggest that parts of sister chromatids move apart during G2 as far as in mitotic chromosomes. This raises the question how cohesin influences the spatial organization of sister chromatids during interphase. To investigate this, we depleted Sororin, which is essential to maintaining sister chromatid cohesion (Schmitz et al., 2007; Ladurner et al., 2016). Transfection of siRNA targeting Sororin induced a pronounced mitotic arrest (Fig. S4, A and B) as previously reported (Rankin et al., 2005), validating efficient target protein depletion. The duration of the preceding interphase, however, was not affected by Sororin RNAi (Fig. S4 C), indicating timely DNA replication. The similar duration of interphase enabled us to directly compare locus separation kinetics in Sororin-depleted and unperturbed control cells. By time-lapse microscopy, we found that Sororin RNAi caused a premature increase of doublets during interphase for all four investigated genomic sites (Fig. 8, A–F; and Fig. S4, D–I), consistent with prior FISH studies (Schmitz et al., 2007; Nishiyama et al., 2010). During late G2, however, the degree of sister locus splitting in control cells approached that of Sororin-depleted cells. Thus, Sororin counteracts sister chromatid separation, but it does not mediate permanent linkage of sister loci at any of the sampled genomic sites.

As for control cells, the distribution of sister locus distances in Sororin-depleted cells fit well to a Rayleigh distribution (Fig. 8 G). The mean distance between sister loci was substantially larger in Sororin-depleted cells compared with control cells at all time points, and it changed only little when cells progressed toward G2 (Fig. 8 H). Hence, premature sister locus separation in Sororin-depleted cells also results in a rapid positional equilibration whereby the average distances between sister loci are higher than in control cells. This is consistent with a lower abundance of cohesion sites between sister chromatids in Sororin-depleted cells.

Discussion

Live-cell imaging of endogenous genomic loci has revealed how sister chromatids resolve during progression from S phase toward mitosis. Our data indicate that the organization of sister chromatids is in part governed by the DNA replication program as previously suggested (Selig et al., 1992). Sister loci separate early after their replication and rapidly equilibrate their distances in dynamic sister chromatid polymers. In a population of G2 cells, early replicating loci hence appear split more frequently compared with late-replicating loci. The probability of sister locus separation also correlates with the nuclear localization and chromatin state, consistent with prior observations that transcriptional silencing counteracts sister locus separation (Azuara et al., 2003). Given that chromatin state and nuclear positioning are highly correlated with DNA replication timing, it is difficult to dissect the relative importance of these genomic features for the kinetics of sister locus separation.

The extensive separation of sister loci during S phase and G2 might result from low abundance of cohesive structures or from potential loop-extrusion activities of cohesin (Fig. 9, A and B). The separation of sister loci might alternatively result from lateral sliding of cohesin along chromatin (Fig. 9 C). In vitro, cohesin can rapidly slide along DNA (Davidson et al., 2016; Stigler et al., 2016), and transcriptional activity can induce relocation of cohesin to distant genomic regions in cells (Lengronne

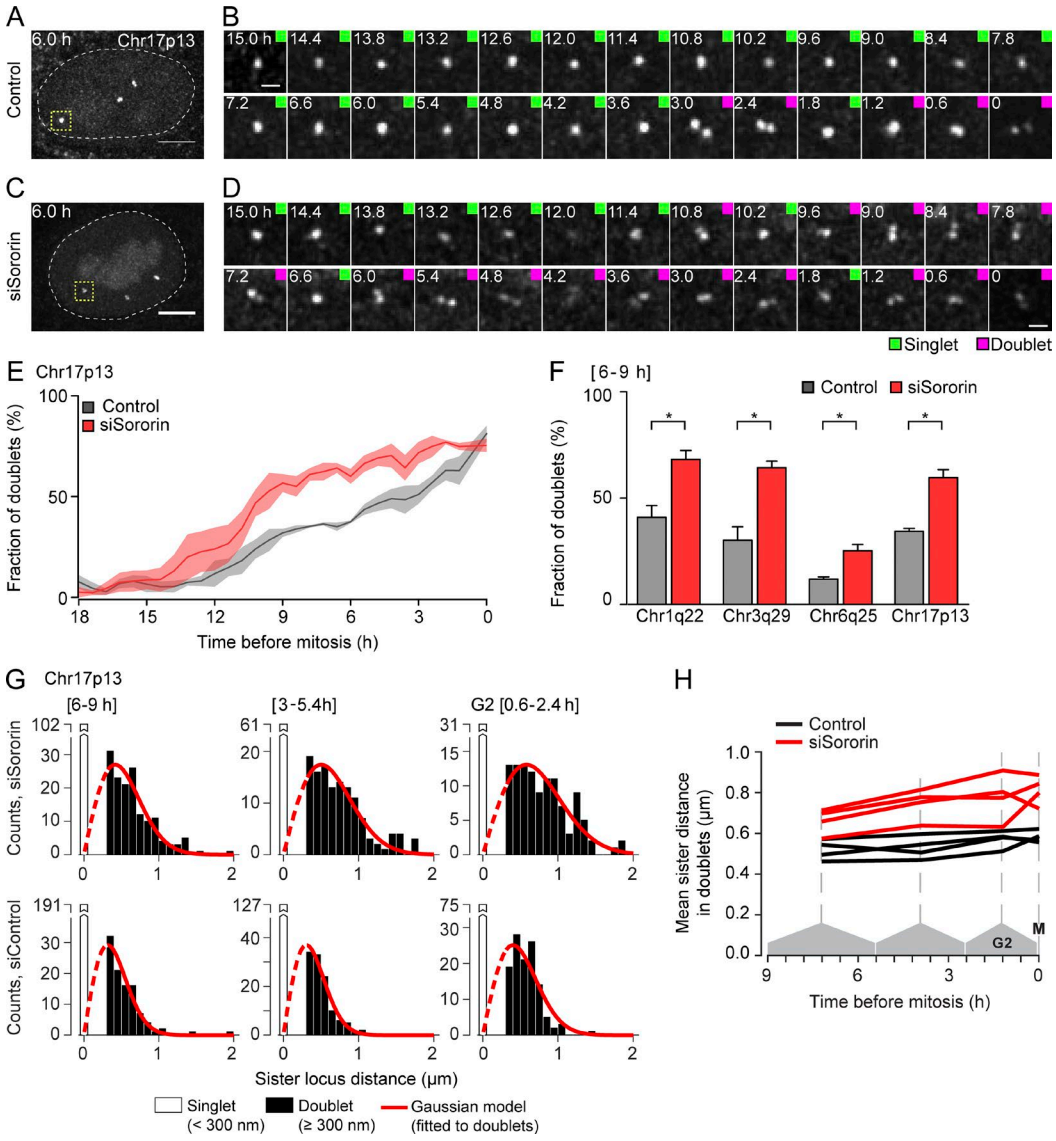

Figure 8. **Sister loci resolve faster in Sororin-depleted cells. (A–D)** Live-cell imaging as in Fig. 1 of the Chr17p13 locus labeled by dCas9-mEGFP/sgRNA after transfection of nontargeting control siRNA (A and B) or Sororin siRNA (C and D). **(A and B)** Maximum-intensity z projection of a control cell (A). Dashed lines indicates nuclear rim, and yellow squares indicate region for trajectory analysis (B). Time is relative to mitosis (t = 0 h). Doublets (magenta) and singlets (green) were annotated automatically as in Fig. 1 (D–H). **(C and D)** Cell transfected with Sororin siRNA analyzed as in A and B. Bars: (A and C) 5 µm; (B and D) 1 µm. **(E)** Fraction of doublets over time based on data shown in A–D. Lines and shaded areas indicate means ± SEM, respectively. n = 3 experiments. **(F)** Fraction of doublets during S phase (6–9 h before mitosis) for data shown in E and for three other genomic sites. *, P = 0.02 for Chr1q22; *, P = 0.02 for Chr3q29; *, P = 0.03 for Chr6q25; *, P = 0.01 for Chr17p13; P-values were derived from two-sided unpaired t tests. n = 3 experiments. **(G)** Distribution of sister locus distances for data shown in E at the indicated cell cycle periods and Rayleigh distributions (corresponding with a Gaussian model) fit to the doublet distance distributions. **(H)** Mean distances between sister loci in doublets for four genomic sites transfected with siRNA targeting Sororin or nontargeting control siRNA.

et al., 2004; Busslinger et al., 2017). It is conceivable that cohesin moves from early toward late-replicating regions of the genome, whereas sister chromatids resolve during interphase progression. The separation of sister loci might further involve a register shift between the two sister chromatids, i.e., with cohesin linking distinct genomic sites in opposing sister chromatids (Fig. 9 D).

Overall, our study uncovers how sister chromatids dynamically reorganize during cell cycle progression. It will be interesting to dissect in future studies how chromatin diffusion, topological constraints by cohesion, and potential loop-extrusion activities jointly shape sister chromatids. It will also be interesting to investigate the organization of sister chromatids close to centromeres, where cohesion persists for the longest time. Our automated assay system and collection of cell lines with labeled endogenous genomic loci will provide a valuable resource to gain further insights into the mechanics underlying chromosome organization.

Materials and methods

Plasmids

For inducible expression of fluorescently tagged catalytically inactive Cas9, the TRE3G-NLS-dCas9-NLS cassette from plasmid pSLQ1658-dCas9-EGFP (51023; Addgene; a gift from B. Huang,

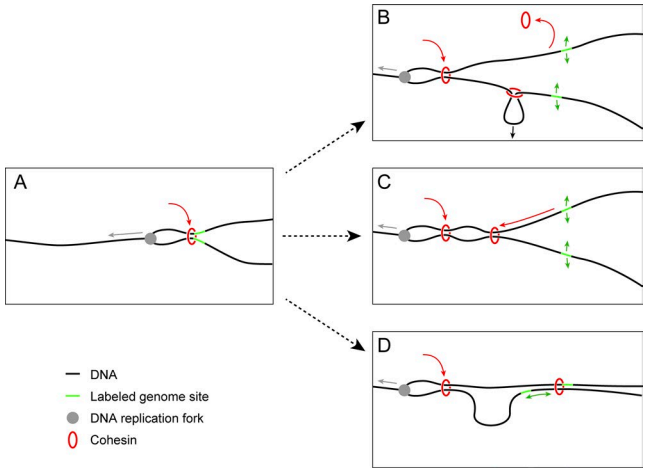

Figure 9. **Models for sister locus separation by cohesin reorganization.** **(A)** Sister chromatid cohesion is established coreplicationally. **(B)** Sister locus separation as a result of cohesin dissociation or cohesin-mediated loop extrusion. **(C)** Sister locus separation as a result of cohesin sliding along DNA. **(D)** Sister locus separation as a result of sister chromatid dealignment.

University of California, San Francisco, San Francisco, CaA; Chen et al., 2013) was tagged with mEGFP and subcloned into the plasmid pQCXIX (631515; Takara Bio Inc.). For the SunTag system, the fluorescently tagged single-chain variable fragment that recognizes GCN4_peptide (scFV-GCN4-sfGFP) was constitutively expressed from plasmid pHR-scFv-GCN4-sfGFP-GB1-NLS-dWPRE (60906; Addgene; Tanenbaum et al., 2014). For inducible expression of nuclear localized dCas9 tagged with 10 copies of GCN4 peptide, the NLS-dCas9-2×NLS-10×GCN4_v4 cassette from plasmid pHRdSV40-dCas9-10×GCN4_v4-P2A-BFP (60903; Addgene) was cloned downstream of the TRE3G promoter in the pHR plasmid backbone from the Addgene 60906 plasmid. For positive clone selection, the plasmid was further modified to contain the blasticidin *S*-transferase gene downstream of the cytomegalovirus promoter (pCMV). For efficient sgRNA expression, the sgRNA tracer sequence optimized for imaging (Chen et al., 2013) was cloned into the LentiCRISPR V1 plasmid (49535; Addgene; Shalem et al., 2014) downstream of the U6 promoter. Additionally, Cas9 and puromycin *N*-acetyltransferase coding sequences from this plasmid were removed and replaced with the sequence coding for rodent thymocyte differentiation antigen Thy1.1 and neomycin phosphotransferase II fusion protein, providing an easy positive clone selection procedure either by FACS or by eukaryotic resistance against geneticin.

sgRNA design

The human tandem repeat database (Gelfand et al., 2007) was bioinformatically screened for unique clusters of at least 20 repeats of an at least 20-nucleotide-long sequence that contained a protospacer-adjacent motif essential for dCas9/sgRNA labeling (with a minimum conservation between repeats of 80%). Only sequences localizing at a minimum distance of 0.5 Mbp from centromeres and telomeres were considered. sgRNA spacers were designed around available protospacer-adjacent motifs avoiding stretches of the same nucleotide and cloned into the sgRNA expression plasmid via BbsI cloning sites as previously described (Cong et al., 2013).

Cell lines and cell culture

WT human HeLa cells (Kyoto strain) were obtained from S. Narumiya (Kyoto University, Kyoto, Japan) and validated by a Multiplex human cell line authentication test (MCA). The human hTERT-RPE1 cell line (further referred as RPE1) was obtained from ATCC. All cells were cultured in in-house–made DMEM supplemented with 2 mmol L-glutamine (Gibco), 10% (vol/vol) FBS (Gibco), and 1% (vol/vol) penicillin-streptomycin (Sigma-Aldrich) and grown in a humidified growth chamber at 37°C and 5% CO_2. All cells lines in this study were regularly tested for mycoplasma contamination, with negative results.

The parental dCas9-mEGFP– and dCas9-10×SunTag–expressing cell lines were derived from human HeLa Kyoto RIEP and RPE1 RIEP cell lines (Samwer et al., 2017) that were modified with rodent-restricted murine ecotropic envelope and allow working with lentivirus at biosafety level 1. Additionally, RIEP cells express Tet3G transactivator protein (Takara Bio Inc.) for doxycycline-inducible gene expression. Cell lines derived from HeLa RIEP and RPE1 RIEP cells were maintained in DMEM with 0.5 µg/ml and 5 µg/ml puromycin (EMD Millipore), respectively. Parental dCas9-mEGFP–expressing HeLa Kyoto and RPE1 cells were generated by J. Jude and M. Roth from the J. Zuber Laboratory (Institute of Molecular Pathology, Vienna, Austria). They used lentivirus-mediated DNA delivery as by Samwer et al. (2017) of the pQCXIX-TRE3G-NLS-dCas9-NLS-mEGFP plasmid packaged in viral particles with EcoR. After viral delivery, a monoclonal dCas9-mEGFP–expressing HeLa cell line was grown from a single colony. The parental dCas9-10×SunTag–expressing HeLa Kyoto cell line was generated using the same lentiviral delivery protocol (Samwer et al., 2017) simultaneously infecting cells with viral particles packaged with pHR-scFv-GCN4-sfGFP-GB1-NLS-dWPRE and pHR-TRE3G-NLS-dCas9-2×NLS-10×GCN4_v4-pCMV-BlastR plasmids. The polyclonal parental cell line was derived by selecting with 2 µg/ml blasticidin S (Sigma-Aldrich). All sgRNA-expressing cell lines were further derived from the parental dCas9-mEGFP– or dCas9-10×SunTag–expressing HeLa and RPE1 cell lines using the same lentiviral delivery protocol (Samwer et al., 2017). Polyclonal cell lines stably expressing locus-specific sgRNA were selected with 1 mg/ml geneticin (Gibco). For uniform mEGFP expression levels in HeLa cells, dCas9-mEGFP expression was induced for 48 h with 1 µg/ml doxycycline (Sigma-Aldrich), and low level–expressing cells were selected using FACS. For all experiments, dCas9 expression was induced for at least 24 h with 1 µg/ml doxycycline in HeLa Kyoto cells and 1 ng/ml doxycycline in RPE1 cells.

Cell synchronization

For mitotic shakeoff, dCas9-mEGFP expression in HeLa cells was induced for 48 h with 1 µg/ml doxycycline (Sigma-Aldrich). 2 h before mitotic shakeoff, dead and arrested cells were removed by mechanical shakeoff and washing cells twice with prewarmed and CO_2-equilibrated PBS. For the next 2 h, cells were grown in prewarmed and CO_2-equilibrated imaging medium (DMEM supplemented with 2 mmol L-glutamine, 10% FBS, and 1%

penicillin-streptomycin but without phenol red and riboflavin). Then, mitotic cells were detached by gently hitting the flask a few times and transferred with the supernatant medium into imaging plates. For fast time-lapse videos, cells were imaged 12–14 h after mitotic shakeoff, corresponding with S phase.

For FISH experiments, cells were synchronized to G2 by a double-thymidine block. First, cells were arrested at the G1/S transition with 2 mM thymidine (Sigma-Aldrich) for 16 h and released into the cell cycle by washing twice with 37°C and CO_2-equilibrated PBS. For the next 8 h, cells were grown in normal DMEM as described above. Cells were then arrested for the second time at the G1/S phase transition by 2 mM thymidine for another 16 h and released into the cell cycle by washing twice with PBS, followed by transfer into DMEM. 6 h after the second release from the thymidine block, cells were in G2 phase as validated by FACS. Throughout the procedure, the medium contained 1 µg/ml doxycycline to maintain dCas9-mEGFP expression.

FACS

FACS was used to derive live cells with uniform mEGFP expression. Cells were sorted in PBS supplemented with 2% (vol/vol) FBS and 2 mM EDTA (AppliChem) in a FACSAria III (BD) flow cytometer. To assess cell synchronization for FISH experiments, DNA content was measured in cells detached from the plate surface using 0.25% trypsin (Thermo Fisher Scientific), washed twice with PBS, and fixed with 73% ice-cold methanol (Sigma-Aldrich) at −20°C overnight. The next day, cells were washed with PBS and stained for 30 min at 37°C in a propidium iodide buffer containing 50 µg/ml propidium iodide (Sigma-Aldrich), 10 mM Tris, pH 7.5 (Sigma-Aldrich), 5 mM $MgCl_2$ (Sigma-Aldrich), and 200 µg RNase A (Thermo Fisher Scientific). Cell cycle profiles were analyzed with a FACSCanto flow cytometer (BD).

siRNA transfection

RNAi-mediated gene silencing was performed by transfecting siRNA using Lipofectamine RNAiMAX (Invitrogen) following the manufacturer's recommendations at room temperature and at a final siRNA concentration of 30 nM. Hs_siSororin (5′-GCCTAGGTGTCCTTGAGCT-3′; Schmitz et al., 2007) was used to deplete Sororin, and siXWneg9 (5′-TACGACCGGTCTATCGTAG-3′; Boni et al., 2015) was used as nontargeting control siRNA. For long-term imaging experiments, 8 × 10^5 cells were seeded in 75-cm^2 flasks and induced with 1 µg/ml doxycycline 24–48 h before imaging. Then, cells were synchronized by mitotic shakeoff as described above. Mitotic and early G1 cells where Sororin is degraded (Rankin et al., 2005; Nishiyama et al., 2010) were further transfected with siRNAs and imaged for the next 24 h. In some experiments, unsynchronized cells were imaged (two to three experiments for chr1q23, one to three experiments for Chr3q29, and one to three experiments for Chr6q29) 16 h after siRNA transfection.

FISH

Oligonucleotide paint probes (Beliveau et al., 2012) were designed to contain a locus-specific sgRNA sequence at their 3′ end and to have 72°C melting temperature (Table S1). To enhance the fluorescent signal, the sequence at the 5′ end was hybridized with a secondary universal probe (5′-CACACGCTC TTCCGTTCTATGCGACGTCGGTGTTTTTTTT-3′). The probes were synthesized at Integrated DNA Technologies with a 5′-conjugated fluorophore (ATTO647N) and purified using HPLC. The secondary probe had conjugates with ATTO647N fluorophores on both sides.

For FISH experiments, cells were grown on Superfrost Ultra Plus slides (Thermo Fisher Scientific) and synchronized to G2 using a double-thymidine block (see above). Cells were fixed with 4% (vol/vol) formaldehyde (Thermo Fisher Scientific) for 10 min, washed with PBS, then with double-concentrated saline–sodium citrate buffer 2×SSCT (0.3 M NaCl buffer, 0.03 M trisodium citrate, and 1% [vol/vol] Tween-20) for 5 min, and then with 2×SSCT buffer containing 50% (vol/vol) formamide (Promega). DNA was denatured in 2×SCCT + 50% (vol/vol) formamide buffer at 92°C for 2 min, and cells were washed for another 20 min at 60°C in the same buffer. Cells were covered with hybriwells (Grace Bio-Labs), and 1.5 µM of both primary and secondary probes were added in 2×SSCT buffer supplemented with 50% (vol/vol) formamide, 10% (wt/vol) dextran sulfate (Sigma-Aldrich), and 20 ng/ml RNase A (Thermo Fisher Scientific). The probes were hybridized in a humidified chamber at 42°C overnight. The next day, the slides were washed in 2×SSCT buffer at 60°C for 15 min, then in the same buffer at room temperature for 10 min, and then were desalted in 0.2× SSC buffer at room temperature for another 10 min. Cell nuclei were stained with 1 µg/ml DAPI (Thermo Fisher Scientific) in 0.2× SSC buffer for 1 h at room temperature. Slides were mounted with the antifade mounting medium Vectashield (Vector Laboratories) and stored at 4°C until imaging.

Microscopy

For all experiments except for the data shown in Fig. S2 (A–F) and Fig. 6 (H and I), cells were imaged with a scanning confocal LSM 780 microscope equipped with a highly sensitive GaAsP detector and a 63× 1.4 NA oil Plan Apochromat objective (ZEISS). Cell nuclei were imaged in 11-µm sections with 0.5 µm z spacing and 101 nm pixel size. For whole–cell cycle videos, the microscope's ZEN 2011 software (ZEISS) was additionally controlled using an open-source macro Autofocuscreen version 3 developed by J. Ellenberg's group (European Molecular Biology Laboratory, Heidelberg, Germany), which automatically directed the microscope to image the same selected locations every 36 min for 24 h and maintained the focus throughout the experiment. Live cells were imaged in chambered coverslips using glass-bottomed LabTek II dishes (Thermo Fisher Scientific) or a plastic-bottomed ibiTreat dishes (Ibidi). Cells were cultured in imaging medium (DMEM supplemented with 10% [vol/vol] FCS and 1% [vol/vol] penicillin-streptomycin but without phenol red and riboflavin to reduce background autofluorescence; Schmitz et al., 2010) supplemented with 1 µg/ml doxycycline.

Cell proliferation and mitotic progression (Fig. S2, A–F) was scored in videos acquired with a widefield ImageXpressMicro XL screening microscope (Molecular Devices) using a 10× 0.5 NA S Fluor dry objective (Nikon). Cells were grown in µCLEAR plastic-bottomed black 96-well imaging plates (Greiner). All cells were treated with 1 µg/ml doxycycline for 48 h before the

start of imaging. 2 h before the start of imaging, cell nuclei were stained with 125 nM SiR-Hoechst DNA dye (Lukinavičius et al., 2015). To assess mitotic duration, cells were imaged every 4.5 min for 24 h. To score cell proliferation, cells were imaged only twice with 24-h intervals.

Fast time-lapse videos for diffusional mobility measurements (Fig. 6, H and I) were acquired with a spinning-disk confocal UltraView Vox AxioObserver (PerkinElmer) using a 150× 1.35 NA glycerol objective (ZEISS) and an electron-multiplying charge-coupled device 9100-13 camera (Hamamatsu Photonics). The microscope was controlled using Volocity software (PerkinElmer). Loci were imaged in seven z slice sections spaced 0.5 µm apart every 0.5 s for 5 min. During imaging, live cells were maintained at 37°C temperature in a humidified 5% CO_2 atmosphere.

Single-allele tracking over the cell cycle

Microscopy images were processed using the open-source software FIJI (version 1.48; ImageJ; National Institutes of Health; Schindelin et al., 2012). dCas9-mEGFP–labeled genomic loci were tracked throughout the cell cycle using a semiautomated FIJI macro (Data S1). The first frame of a mitotic cell was manually identified by cell rounding and dispersion of nuclear dCas9-mEGFP signal after nuclear envelope breakdown. Then, two randomly selected individual alleles from each cell were tracked from the beginning of the video until the following mitosis. Only alleles that were at least 3 µm away from other labeled alleles were considered. 30 × 30–pixel images were cropped and saved for further processing from a single z plane rather than the maximum-intensity projection of all z sections. In case a labeled locus was visible in several z sections, the slice where two sister loci were visible was selected; otherwise, the z slice with the brightest fluorescence signal was selected. If two fluorescent dots were visible in separate z sections and it was not possible to distinguish whether they were two individual sister loci or a single fluorescent dot recorded twice because of its motion, these frames were omitted from the analysis to avoid false-positive singlet detection.

Quantification of interchromatid distances and the fraction of split

Sister chromatid distance was measured using a custom-developed R script (Data S2) based on packages seqinr (Charif and Lobry, 2007), spatstat (Baddeley et al., 2015), and SDMTools (VanDerWal et al., 2011). Original images were converted into text images using FIJI. The shot noise was then reduced using 0.8-pixel-diameter Gaussian blur and further removed by subtracting 95% of the lowest pixel values. The interchromatid distance in the images was measured by fitting a mixture of two 2D Gaussian functions:

$$G(x, y) = z_1 \frac{1}{\sigma\sqrt{2\pi}} e^{-\frac{(x-x_1)^2+(y-y_1)^2}{2\sigma^2}} + z_2 \frac{1}{\sigma\sqrt{2\pi}} e^{-\frac{(x-x_2)^2+(y-y_2)^2}{2\sigma^2}};$$

where x_1, y_1 and x_2, y_2 are the center positions of two sister loci, respectively, z_1 and z_2 are amplitudes of the two Gaussian functions approximating the fluorescence intensities of two fluorescent foci, and σ^2 is the variance of a single Gaussian function, an approximation for the diameter of the microscope's point spread function. It was assumed that two sister loci are present in doublet as well as singlet images and therefore that a mixture to two 2D Gaussian functions was fitted to all the images. The differences in signal intensity between sister loci was limited to threefold ($z_2 \geq 0.33z_1$). Additionally, it was assumed that both sister loci are of the same diameter and are symmetrical in x and y directions ($\sigma = \sigma_{x1} = \sigma_{y1} = \sigma_{x2} = \sigma_{y2}$). The 2D Gaussian variance σ^2 was measured experimentally by fitting a single 2D Gaussian function:

$$G(x, y) = z \frac{1}{\sigma\sqrt{2\pi}} e^{-\frac{(x-x_1)^2+(y-y_1)^2}{2\sigma^2}}$$

to images of 100-nm-diameter fluorescent beads acquired with the same microscopy settings. To initialize the fitting procedure, approximate center positions of the fluorescent foci were calculated as the coordinates of the two highest local maxima. It was visually monitored whether both detected local maxima were inside fluorescent foci. If a single bright noise pixel was detected as a maximum, no measurements were recorded. For this, the cell cycle stage was blinded. A mixture of two 2D Gaussian functions was optimized using least square regression analysis.

Microscopy image simulations to validate spot detection method

To test the accuracy of the image analysis method for quantification of sister locus distances, we simulated microscopy images with two fluorescent dots (related to Fig. S3) using Python. First, the positions of the simulated sister loci (μ_x and μ_y) were randomly generated within the constrained circular area of 0.3, 0.5, or 0.75 µm diameter. The point spread function of the microscope was approximated with a 2D Gaussian function:

$$G(x, y) = A^* e^{-\frac{(x-\mu_x)^2+(y-\mu_y)^2}{2\sigma^2}} + offset + Noise.$$

Mean amplitude A (intensity) ± SD and mean variance σ^2 ± SD for the 2D Gaussian function were calculated from fits of actual microscopy images of Chr3q29 locus. The noise in the images was simulated by inverse transform sampling, i.e., drawing a random value for each pixel from the distribution of the noise intensities in actual microscopy images of Chr3q29 locus. Simulated images were further used to determine the center positions of the two fluorescent dots using the mixture of two 2D Gaussian functions (see above).

Quantification of locus distance to the genomic cohesin or Sororin enrichment site

Genomic positions of SMC3 and Sororin enrichments sites were calculated for ChIP-seq data from HeLa Kyoto cells synchronized to G2 (Ladurner et al., 2016). Peaks were filtered with a p-value threshold of $1e^{-10}$ after peak calling with MACS 1.4.2 algorithm (Zhang et al., 2008) and annotated if present in two independent experimental replicates. Genomic distances were calculated between the center of each fluorescently labeled locus (center position of sgRNA target region) and the center of the nearest SMC3 or SMC3/Sororin ChIP-seq peak, respectively, based on GRCh37/hg19 genome assembly.

Quantification of nuclear positioning for dCas9-mEGFP–labeled loci

The distance of dCas9-mEGFP–labeled loci from the nuclear periphery was measured during S phase (15 h after mitosis) using confocal long-term imaging data of the entire cell cycle. The distance of dCas9-mEGFP–labeled loci and the nuclear rim (based on nucleoplasmic background fluorescence) was manually measured using the FIJI point tool in a single z section. All visible alleles were measured in a given cell. Two bottom and two top z sections (1.4 µm each) of the nucleus were omitted as the nuclear edge could not be accurately detected along the z axis owing to the low z sampling rate. For doublets, the center position was used to calculate the distance to the nuclear rim.

Quantification of histone modification and transcriptional activity

Histone modification data for HeLa cells were obtained from ENCODE Project Consortium (2012). Gene Expression Omnibus (GEO) sample accession numbers for individual modifications are as follows: H3K9me3 (GSM1003480), H3K27me3 (GSM733696), H3K4me3 (GSM733682), H3K9ac (GSM733756), and H3K27ac (GSM733684). Greater than or less than 50 kb regions from the centers of the labeled repeats were analyzed for the presence of relevant histone modifications. The region was considered positive for the modification if a single peak with p-value smaller than the threshold of $1e^{-11}$ was present.

Transcriptional activity in the same ±50-kb regions around the centers of the labeled repeats was analyzed from polyadenylated RNA sequencing dataset in HeLa cells (ENCODE Project Consortium, 2012) with GEO sample number GSM958735. The region was considered positive for transcription if at least one locus in the region was detected in two experimental replicates with a density of two reads per million.

Replication timing of the labelled repeats was determined in HeLa cells from the newly replicated DNA element sequencing dataset (Hansen et al., 2010; ENCODE Project Consortium, 2012) with GEO sample number GSM923449.

Quantification of labeled allele numbers in each cell line

The number of the fluorescent foci was counted in live-cell 3D confocal images extracted from long-term videos (12–18 h after mitosis corresponding with S/G2 phase). Cell nuclei were observed in multiple time frames, and the number of fluorescent nucleoplasmic foci that were visible in at least three time points were counted. If two fluorescent foci were <2 µm apart and changed from a doublet to a singlet appearance over time, they were considered to be sister loci of the same replicated chromosome and were counted as a single allele.

Quantification of cell proliferation and mitotic timing

Cell proliferation was assessed as fold change in cell number in 24 h. Cell numbers were manually counted using the cell counter plugin in FIJI. Mitotic duration was scored manually by counting the number of time frames with chromatin morphologies specific to mitosis (from prophase to anaphase).

Quantification of signal intensity at dCas9-mEGFP– and dCas9-SunTag–labeled loci

Stable cell lines with dCas9-mEGFP and dCas9-SunTag labeling the Chr17p13 locus were imaged using identical microscopy conditions. The mean fluorescence intensity of a 6 × 6–pixel region of interest around a labeled locus was measured as signal. A mean fluorescence intensity of five mean fluorescence intensity measurements at randomly selected locations in the nucleus using same-sized region of interest was measured as nucleoplasmic background and subtracted from the signal.

Dynamic equilibrium model for sister chromosomes

To model sister chromosomes after replication, we assumed two polymers that are linked by cohesin at specific linkage points along the genome. The section between two linkage points was thus a polymer ring. The two sister loci labeled in our experimental tracking data corresponded with two specific positions on this ring.

In thermodynamic equilibrium, the distribution of relative positions of two monomers in an ideal polymer ring is a 3D Gaussian (Khokhlov and Grosberg, 1994). In a 2D projection, like our microscopy data, the distribution of relative positions is a 2D Gaussian, $p(r) = 1/(2\,\pi\,s^2)\ exp(-r^2/2s^2)$, where r is 2D vector connecting sister loci positions and s is the scale of the distribution. Integrating out the angular orientation, one obtains for the distribution of relative distances $d = |r|$ the Rayleigh distribution $p(d) = d/s^2\ exp(-d^2/2s^2)$.

Our assumption of thermodynamic equilibrium is based on our findings that (a) neither the fraction of doublets after the first doublet occurrence nor (b) the mean sister distance in doublets increases significantly over time, consistent with a picture in which sister loci equilibrate after replication on a timescale that is fast compared with cell cycle times and also consistent with the analysis of mean square displacements. A posteriori, our assumption is validated by a good agreement between our equilibrium model and the data.

Our assumption of ideal polymer rings relies on the Flory theorem in polymer physics, which states that excluded volume effects can be neglected in a dense melt of polymers, which is a reasonable approximation for chromatin in the cell nucleus.

Histograms of sister distances and fit by Rayleigh distributions

Measured sister distances across several time points were accumulated as indicated by the cell cycle periods in Fig. 6 F. We then binned these data in 100-nm bins. All distances <300 nm were classified as singlets owing to limited microscopy resolution (see Fig. S2, G–L). We fitted the data with Rayleigh distributions with an additional numerical prefactor A, namely $p(d,s,A) = A\ d/s^2\ exp(-d^2/2s^2)$. We introduced the prefactor A instead of normalizing the distribution of distances to unity to preserve the information on sample numbers in the histogram plots. For fitting, we used only doublets (bins with diameters of >300 nm) centered at the respective bin midpoints (350 nm, 450 nm, et cetera). We then minimized the sum of squared differences between $p(d,s,A)$ and the binned data over the parameters A and s. Mean sister locus distances in Fig. 6 (F and G) were computed only for doublets (data with diameters >300 nm).

Mean square displacements and diffusional mobility analysis

RMSDs were computed from tracking data of videos recorded with two frames per second. The 2D positions of sister loci were automatically determined in maximum-intensity projection images by fitting mixtures of two Gaussian functions (see above). Individual sister loci were tracked using nearest-neighbor tracking by minimizing the sum of both sister loci displacements in two consecutive frames. Diffusional mobility analysis was then performed on consecutive frames where sister loci appeared as doublets. Trajectory segments of doublets were determined by the following data preprocessing: First, we detected frames where tracking did not detect the loci. For up to three consecutive failures, we interpolated the coordinates from before and after the failures; otherwise runs were segmented. Second, in some cases, the tracking coordinates had unusually large jumps (>600 nm). When a trajectory jumped back near the prior coordinates right after a large jump, we considered this jump an outlier and interpolated coordinates between before and after the jump; otherwise, runs were segmented.

To compute mean square displacements, we collected all runs of doublets in the preprocessed data. Only doublet runs of a minimal length of 10 s (21 frames) were used. Within such runs, both sister loci were used to compute RMSDs. For each sister locus in a given run, squared displacements (*SDs*) for a given time shift between two frames *dt* were computed as $SD(dt) = (x_{i+dt} - x_i)^2 + (y_{i+dt} - y_i)^2$, where *x* and *y* are estimated center positions of a single sister locus at *i* and *i + dt* time points. Squared displacements were accumulated for all valid starting frames $i = 1...L - dt$ and across both sister loci across all doublet runs across all recorded videos. Finally, $RMSD(dt)$ was obtained by dividing the accumulated $sum(SD[dt])$ by the number of $SD(dt)$ for the given *dt*. We show RMSDs only up to 50 s because larger times are dominated by a few or only one long doublet run.

Anomalous diffusion coefficients *D* and exponents α in the relation $RMSD(dt) = D \times t^{l/2}$ were obtained by linear fits of $\log_{10}$(RMSD) versus $\log_{10}$(dt) plots. For the linear fits, RMSDs from $t\_min\_fit = 0.5\ s$ to $t\_max\_fit = 10\ s$ were used.

Sample numbers

The split kinetics of the labeled locus was characterized by imaging untreated (Figs. 2, 6, and S3) or Sororin-depleted and control (Figs. 8 and S4) cells over the cell cycle every 36 min. For each locus, these experiments were repeated three times ($n \geq 5$ cells per experiment) except untreated Chr1q22, and Chr3q29 and Sororin-depleted Chr1q22, Chr3q29, and Chr6q25 loci were imaged four times, and two replicas were merged into one experiment when calculating the fraction of doublets because of insufficient cell numbers. In these experiments, cells were synchronized using mitotic shakeoff (see above), except in one out of three replicates for untreated Chr1q22, Chr3q29, Chr4q35b, Chr6q25, Chr7q36, and Chr17p13 loci, cells were growing asynchronously. In Sororin-depletion experiments in two to three experiments for Chr1q23, in one to three experiments for Chr3q29, and in one to three experiments for Chr6q29, cells were growing asynchronously.

For G2, interchromatin distance measurements were pooled from four time points (0.6–2.4 h) before mitosis, resulting in the following combined sample numbers from three experiments for untreated HeLa cells: Chr1p36 ($n = 207$), Chr1q22 ($n = 288$), Chr1q42 ($n = 205$), Chr2q14 ($n = 147$), Chr3q29 ($n = 242$), Chr4q34 ($n = 201$), Chr4q35a ($n = 165$), Chr4q35b ($n = 223$), Chr6q25 ($n = 196$), Chr7q36 ($n = 243$), Chr8p21 ($n = 179$), Chr10p13 ($n = 220$), Chr10q26 ($n = 150$), Chr11p15 ($n = 232$), Chr12q24 ($n = 184$), and Chr17p13 ($n = 264$); and for hTERT-RPE1 cells: Chr1p36 ($n = 190$), Chr3q29 ($n = 184$), Chr4q35b ($n = 204$), Chr6q25 ($n = 304$), and Chr17p13 ($n = 235$). From these data, a subset of interchromatid distances was randomly sampled for every locus to enable unbiased data visualization and comparison of different loci ($n = 120$ for Fig. 2 B, and $n = 100$ for Fig. 3 E). The fraction of doublets in G2 cells was calculated in each of the three experiments ($n \geq 30$ interchromatid distance measurements each) and is presented as mean ± SEM (Figs. 2 D, 3 F, 4 [B and D], and 5 [D, F, and G]). For Fig. 2 C, mitotic distances were measured in a single frame of untreated cells in mitosis in three experiments, resulting in the combined sample numbers: Chr1p36 ($n = 34$), Chr1q22 ($n = 48$), Chr1q42 ($n = 38$), Chr2q14 ($n = 33$), Chr3q29 ($n = 33$), Chr4q34 ($n = 40$), Chr4q35a ($n = 31$), Chr4q35b ($n = 37$), Chr6q25 ($n = 23$), Chr7q36 ($n = 45$), Chr8p21 ($n = 31$), Chr10p13 ($n = 33$), Chr10q26 ($n = 31$), Chr11p15 ($n = 33$), Chr12q24 ($n = 42$), and Chr17p13 ($n = 44$). From these data, the fraction of doublets in mitosis was calculated from $n \geq 7$ interchromatid distance measurements from each of the three experiments and is presented as mean ± SEM (Fig. 2 E).

For S phase, interchromatin distance measurements were pooled from six time points (6–9 h) before mitosis, resulting in the following combined sample numbers from all experiments: Chr1q22 ($n_{control} = 345$ and $n_{siSororin} = 294$), Chr3q29 ($n_{control} = 212$ and $n_{siSororin} = 220$), Chr6q25 ($n_{control} = 285$ and $n_{siSororin} = 575$), and Chr17p13 ($n_{control} = 292$ and $n_{siSororin} = 254$). The fraction of doublets in S phase was calculated from $n \geq 35$ interchromatid distance measurements per condition per locus per experiment and is presented as mean ± SEM (Fig. 8 F).

The fraction of doublets through the entire cell cycle was calculated from ≥10 interchromatid distance measurements in a sliding window of three time points (except mitosis; $t = 0$) and is presented as mean ± SEM at each time point (middle of the sliding window; Figs. 6 D, 7 A, 8 E, S3, and S4 [D, F, and H]). Cumulative histograms of the first detected doublet were calculated from the longest and most complete trajectories pooled from three experiments: $n = 40$ trajectories (Figs. 6 D, 7 B, and S3) and $n = 30$ trajectories (Fig. S4, E, G, and I). 20 longest and most complete trajectories from three experiments are shown in Figs. 6 C and S3. The fraction of doublets after the initial split was calculated from the data as in Figs. 6 (C and D) and S3 from at least five measurements per time point per experiment in three independent experiments and is presented as mean ± SEM in Fig. 6 E and from at least 10 measurements per time point merged from three experiments in Fig. 7 D.

In Figs. 6 (F and G) and 8 (G and H), measurements from indicated time points from three experiments were merged together: six time points for 6–9 h, six time points for 3–5.4 h, and four time points for G2 (0.6–2.4 h). In Fig. 6 (F and G), sample numbers for individual cell cycle stages are as follows: 6–9 h, $n = 302$ ($n_{singlet} = 222$ and $n_{doublet} = 80$), 3–5.4 h, $n = 311$ ($n_{singlet} = 187$ and $n_{doublet} =$

124), and G2, $n = 260$ ($n_{singlet} = 141$ and $n_{doublet} = 119$). In Fig. 8 G, sample numbers for individual cell cycle stages are as follows: for control treatment in 6–9 h, $n = 292$ ($n_{singlet} = 191$ and $n_{doublet} = 101$), in 3–5.4 h, $n = 242$ ($n_{singlet} = 127$ and $n_{doublet} = 115$), and in G2, $n = 194$ ($n_{singlet} = 75$ and $n_{doublet} = 119$); for Sororin-depleted cells in 6–9 h, $n = 253$ ($n_{singlet} = 102$ and $n_{doublet} = 151$), in 3–5.4 h, $n = 188$ ($n_{singlet} = 61$ and $n_{doublet} = 127$), and in G2, $n = 142$ ($n_{singlet} = 31$ and $n_{doublet} = 111$).

In Fig. 6 I, for mean square displacement measurements, cells were imaged in two independent experiments resulting in the following combined sample numbers: Chr1q22 ($n = 44$ trajectories from 26 cells), Chr3q29 ($n = 51$ trajectories from 31 cells), Chr6q25 ($n = 56$ trajectories from 40 cells), and Chr17p13 ($n = 58$ trajectories from 37 cells).

For Fig. 5 C, the sample numbers for nuclear positioning measurements are as follows: Chr1p36 ($n = 207$), Chr1q22 ($n = 288$), Chr1q42 ($n = 205$), Chr2q14 ($n = 147$), Chr3q29 ($n = 242$), Chr4q34 ($n = 201$), Chr4q35a ($n = 165$), Chr4q35b ($n = 223$), Chr6q25 ($n = 196$), Chr7q36 ($n = 243$), Chr8p21 ($n = 179$), Chr10p13 ($n = 220$), Chr10q26 ($n = 150$), Chr11p15 ($n = 232$), Chr12q24 ($n = 184$), and Chr17p13 ($n = 264$).

For Fig. 3, FISH was repeated in six independent experiments except for Chr17p13 ($n = 3$), resulting in the following combined numbers of interchromatid measurements from all the experiments: Chr1q22 ($n_{WT} = 600$ and $n_{Chr1q22} = 469$), Chr3q29 ($n_{WT} = 607$ and $n_{Chr3q29} = 505$), Chr4q35b ($n_{WT} = 591$ and $n_{Chr4q35b} = 512$), Chr6q25 ($n_{WT} = 856$ and $n_{Chr6q25} = 799$), Chr7q36 ($n_{WT} = 507$ and $n_{Chr7q36} = 441$), and Chr17p13 ($n_{WT} = 239$ and $n_{Chr17p13} = 326$). For unbiased visualization, a subset of these data ($n = 230$) was randomly sampled (Fig. 3 C). The fraction of doublets was calculated in each experiment from $n \geq 34$ measurements and is presented as mean ± SEM in Fig. 3 D.

For Fig. S1, the numbers of labeled alleles for each locus were counted in indicated numbers of cells: Chr1p36 ($n = 36$), Chr1q22 ($n = 31$), Chr1q42 ($n = 33$), Chr2q14 ($n = 26$), Chr3q29 ($n = 40$), Chr4q34 ($n = 39$), Chr4q35a ($n = 46$), Chr4q35b ($n = 29$), Chr6q25 ($n = 41$), Chr7q36 ($n = 10$), Chr8p21 ($n = 43$), Chr10p13 ($n = 42$), Chr10q26 ($n = 36$), Chr11p15 ($n = 44$), Chr12q24 ($n = 40$), and Chr17p13 ($n = 25$).

For Fig. S2 E, the numbers of cells were counted at time point 0 and at 24 h in three independent experiments, resulting in the following combined numbers of cells: WT HeLa Kyoto ($n_{0h} = 742$ and $n_{24h} = 1,655$), dCas9-mEGFP parental cell line ($n_{0h} = 657$ and $n_{24h} = 1,575$), Chr1q22 ($n_{0h} = 750$ and $n_{24h} = 1,741$), Chr1q4 ($n_{0h} = 466$ and $n_{24h} = 1,079$), Chr4q35b ($n_{0h} = 601$ and $n_{24h} = 1,419$), Chr6q25 ($n_{0h} = 680$ and $n_{24h} = 1,502$), Chr7q36 ($n_{0h} = 567$ and $n_{24h} = 1,219$), Chr10p13 ($n_{0h} = 660$ and $n_{24h} = 1,534$), Chr10q26 ($n_{0h} = 508$ and $n_{24h} = 1,236$), and Chr17p13 ($n_{0h} = 558$ and $n_{24h} = 1,280$). For Fig. S2 F, $n = 3$ experiments and 30 cells each. For Fig. S2 O, $n_{dCas9\text{-}mEGFP} = 26$ cells and $n_{dCas9\text{-}SunTag} = 25$ cells, resulting in combined number of labeled loci quantified: $n_{dCas9\text{-}mEGFP} = 76$ and $n_{dCas9\text{-}SunTag} = 75$. For Fig. S2 L, $n = 10,800$ images were simulated.

For Fig. S4 B, the number of Chr17p13 cells arrested in mitosis was calculated from three independent experiments, resulting in combined numbers of $n = 98$ cells in control and $n = 110$ cells in siSororin treatment. For Fig. S4 C, the cumulative histogram of the cell cycle duration is calculated for Chr17p13 locus from three experiments with the following combined cell numbers: $n_{control} = 137$ and $n_{siSororin} = 167$.

Statistical analysis

All statistical tests were performed with R software (3.1.2) using stats and lawstat packages. The normality of data distribution was tested using Kolmogorov-Smirnov tests, and the variance was tested using Levene tests.

For two groups of normally distributed data, two-sided unpaired Welch's *t* tests were performed: in Fig. 5 E, P = 0.02; in Fig. 5 F, P = 0.02; in Fig. 5 G, P = 0.10; in Fig. 5 H, P = 0.01; in Fig. 5 I, P = 0.10; in Fig. 5 J, P = 0.17; in Fig. 5 K, P = 0.07; in Fig. 5 L, P = 0.02; in Fig. 5 M, $P = 3.0 \times 10^{-3}$; in Fig. 8 F, Chr1q22, P = 0.02, Chr3q29, P = 0.02, Chr6q25, P = 0.03, and Chr17p13, P = 0.01; in Fig. S2 O, $P = 4.2 \times 10^{-10}$; and in Fig. S4 B, P = 0.01. Three and more groups of normally distributed data were tested with one-way ANOVA not assuming equal variance: in Fig. 2 D, $P = 6.8 \times 10^{-8}$; in Fig. 2 E, P = 0.75; in Fig. 3 D, $P_{wt} = 3.9 \times 10^{-8}$; in Fig. S2 E, P = 0.12; and in Fig. S2 F, P = 0.97.

Two groups of abnormally distributed data were compared using two-sided unpaired Wilcoxon rank sum tests: in Fig. 3 C, Chr1q22, P = 0.80, Chr3q29, P = 0.23, Chr4q35b, P = 0.85, Chr6q25, P = 0.33, Chr7q36, P = 0.12, and Chr17p13, P = 0.33. More than three groups of not normally distributed data were compared using Kruskal-Wallis rank sum test: in Fig. 5 C, $P < 2.2 \times 10^{-16}$.

Data plotting

All data were plotted using R software using graphics and beeswarm packages except for Figs. 6 (F–I) and 8 (G and H), in which data were plotted using MatLab (R2017b; MathWorks). All microscopy images for the figures were processed with FIJI using Gaussian blur denoising (0.8-pixel diameter) and cropping or projections as indicated. ChIP-seq tracks for SMC3 and Sororin were visualized with integrated genome viewer (IGV 2.3.66; Robinson et al., 2011).

Online supplemental material

Fig. S1 shows example confocal images of representative live cells for all cell lines with dCas9-mEGFP/sgRNA–labeled loci. Bar graphs represent allele counts for each cell line. Fig. S2 (A–F) shows that cell proliferation and mitotic duration in dCas9-labeled cell lines are similar to WT unlabeled cells. Fig. S2 (G–L) shows the accuracy of the 2D Gaussian mixture model–fitting procedure in measuring interchromatid distances. Fig. S2 (M–O) shows the comparison of signal-to-noise intensities of dCas9-mEGFP– versus dCas9-SunTag–labeled Chr17p13 loci in live cells. Fig. S3 shows the kinetics of sister locus resolution from S phase until mitosis for 15 labeled loci. Fig. S4 (A–C) shows that cells depleted of Sororin arrest in mitosis but do not significantly prolong interphase. Fig. S4 (D–I) shows the kinetics of sister locus resolution after control treatment and Sororin RNAi for three genomic sites. Table S1 shows the genomic positions and genomic features of the dCas9-mEGFP/sgRNA–labeled loci. Data S1 is a FIJI macro for semiautomated tracking of individual alleles. Data S2 is an R script for Gaussian fitting procedure to determine labeled locus positions.

Acknowledgments

The authors thank A. Schleiffer for providing the list of unique repeat sites in the human genome, B. Huang for dCas9-EGFP and

gRNA plasmids, H. Zuber, J. Jude, and M. Roth for dCas9-mEGFP HeLa and hTERT-RPE1 cells, M. Mitter and L. Mirny for comments on the manuscript, Vienna BioCenter Core Facilities BioOptics and Bioinformatics core facilities for technical support, and Life Science Editors for editing assistance. The authors also thank ENCODE Consortiom for histone modification datasets in HeLa cells generated by the B.E. Bernstein Laboratory, polyadenylated RNA sequencing dataset generated by B. Wold, R. Myers, Illumina gene expression, and TopHat/Cufflinks development groups, and for replication timing dataset generated by the University of Washington ENCODE group.

Research in the laboratory of D.W. Gerlich has been supported by the European Commission's FP7/2007-2013 under grant agreements 241548 (MitoSys) and 258068 (Systems Microscopy), by a European Research Council starting grant (281198), by the Wiener Wissenschafts-, Forschungs- und Technologiefonds (LS14-009), and by the Austrian Science Fund (Austrian Science Fund special research program Chromosome Dynamics; SFB F34-06). Research in the laboratory of J.-M. Peters has been supported by Boehringer Ingelheim, a European Research Council advanced grant CohesinMolMech, the Austrian Science Fund (Austrian Science Fund special research program SFB F34 Chromosome Dynamics and Wittgenstein award Z196-B20), and the Austrian Research Promotion Agency (Headquarter grant FFG-834223). R. Stocsits received a PhD fellowship from the Boehringer Ingelheim Fonds. J. Nuebler received financial support from the National Science Foundation under grant 1504942 (Physics of Chromosomes) and the National Institutes of Health under grant GM114190 (Polymer Models of Mitotic and Interphase Chromosomes).

The authors declare no competing financial interests.

Author contributions: Conceptualization: D.W. Gerlich, R. Stanyte (lead), and J.-M. Peters (supporting). Data curation: R. Stocsits. Formal analysis: R. Stanyte (lead), J. Nuebler, R. Hoefler, and R. Stocsits (supporting). Funding acquisition: D.W. Gerlich and R. Stanyte. Investigation: R. Stanyte (lead) and C. Blaukopf (supporting). Methodology: R. Stanyte (lead) and J. Nuebler (supporting). Project administration and supervision: D.W. Gerlich. Visualization: R. Stanyte (lead), J. Nuebler, and R. Hoefler (supporting). Writing: D.W. Gerlich (lead) and R. Stanyte (supporting).

Submitted: 23 January 2018
Revised: 16 March 2018
Accepted: 11 April 2018

References

Azuara, V., K.E. Brown, R.R.E. Williams, N. Webb, N. Dillon, R. Festenstein, V. Buckle, M. Merkenschlager, and A.G. Fisher. 2003. Heritable gene silencing in lymphocytes delays chromatid resolution without affecting the timing of DNA replication. *Nat. Cell Biol.* 5:668–674. https://doi.org/10.1038/ncb1006

Baddeley, A., E. Rubak, and R. Turner. 2015. Spatial Point Patterns: Methodology and Applications with R. Chapman and Hall/CRC Press, London.

Beliveau, B.J., E.F. Joyce, N. Apostolopoulos, F. Yilmaz, C.Y. Fonseka, R.B. McCole, Y. Chang, J.B. Li, T.N. Senaratne, B.R. Williams, et al. 2012. Versatile design and synthesis platform for visualizing genomes with Oligopaint FISH probes. *Proc. Natl. Acad. Sci. USA.* 109:21301–21306. https://doi.org/10.1073/pnas.1213818110

Bhardwaj, S., M. Schlackow, M. Rabajdova, and M. Gullerova. 2016. Transcription facilitates sister chromatid cohesion on chromosomal arms. *Nucleic Acids Res.* 44:6676–6692. https://doi.org/10.1093/nar/gkw252

Bickmore, W.A., and B. van Steensel. 2013. Genome architecture: domain organization of interphase chromosomes. *Cell.* 152:1270–1284. https://doi.org/10.1016/j.cell.2013.02.001

Boni, A., A.Z. Politi, P. Strnad, W. Xiang, M.J. Hossain, and J. Ellenberg. 2015. Live imaging and modeling of inner nuclear membrane targeting reveals its molecular requirements in mammalian cells. *J. Cell Biol.* 209:705–720. https://doi.org/10.1083/jcb.201409133 26056140

Busslinger, G.A., R.R. Stocsits, P. van der Lelij, E. Axelsson, A. Tedeschi, N. Galjart, and J.-M. Peters. 2017. Cohesin is positioned in mammalian genomes by transcription, CTCF and Wapl. *Nature.* 544:503–507. https://doi.org/10.1038/nature22063

Charif, D., and J.R. Lobry. 2007. SeqinR 1.0-2: A Contributed Package to theR Project for Statistical Computing Devoted to Biological SequencesRetrieval and Analysis. In Structural Approaches to Sequence Evolution. Biological and Medical Physics, Biomedical Engineering. U. Bastolla, M. Porto, H.E. Roman, and M. Vendruscolo, editors. Springer, Berlin, Heidelberg. 207–232.

Chen, B., L.A. Gilbert, B.A. Cimini, J. Schnitzbauer, W. Zhang, G.-W. Li, J. Park, E.H. Blackburn, J.S. Weissman, L.S. Qi, and B. Huang. 2013. Dynamic imaging of genomic loci in living human cells by an optimized CRISPR/Cas system. *Cell.* 155:1479–1491. https://doi.org/10.1016/j.cell.2013.12.001

Cong, L., F.A. Ran, D. Cox, S. Lin, R. Barretto, N. Habib, P.D. Hsu, X. Wu, W. Jiang, L.A. Marraffini, and F. Zhang. 2013. Multiplex genome engineering using CRISPR/Cas systems. *Science.* 339:819–823. https://doi.org/10.1126/science.1231143

Davidson, I.F., D. Goetz, M.P. Zaczek, M.I. Molodtsov, P.J. Huis In 't Veld, F. Weissmann, G. Litos, D.A. Cisneros, M. Ocampo-Hafalla, R. Ladurner, et al. 2016. Rapid movement and transcriptional re-localization of human cohesin on DNA. *EMBO J.* 35:2671–2685. https://doi.org/10.15252/embj.201695402

Dixon, J.R., S. Selvaraj, F. Yue, A. Kim, Y. Li, Y. Shen, M. Hu, J.S. Liu, and B. Ren. 2012. Topological domains in mammalian genomes identified by analysis of chromatin interactions. *Nature.* 485:376–380. https://doi.org/10.1038/nature11082

ENCODE Project Consortium. 2012. An integrated encyclopedia of DNA elements in the human genome. *Nature.* 489:57–74. https://doi.org/10.1038/nature11247

Fudenberg, G., M. Imakaev, C. Lu, A. Goloborodko, N. Abdennur, and L.A. Mirny. 2016. Formation of Chromosomal Domains by Loop Extrusion. *Cell Reports.* 15:2038–2049. https://doi.org/10.1016/j.celrep.2016.04.085

Gassler, J., H.B. Brandão, M. Imakaev, I.M. Flyamer, S. Ladstätter, W.A. Bickmore, J.-M. Peters, L.A. Mirny, and K. Tachibana. 2017. A mechanism of cohesin-dependent loop extrusion organizes zygotic genome architecture. *EMBO J.* 36:3600–3618. https://doi.org/10.15252/embj.201798083

Gelfand, Y., A. Rodriguez, and G. Benson. 2007. TRDB--the Tandem Repeats Database. *Nucleic Acids Res.* 35(Database):D80–D87. https://doi.org/10.1093/nar/gkl1013

Gerlich, D., B. Koch, F. Dupeux, J.-M. Peters, and J. Ellenberg. 2006. Live-cell imaging reveals a stable cohesin-chromatin interaction after but not before DNA replication. *Curr. Biol.* 16:1571–1578. https://doi.org/10.1016/j.cub.2006.06.068

Giménez-Abián, J.F., D.J. Clarke, A.M. Mullinger, C.S. Downes, and R.T. Johnson. 1995. A postprophase topoisomerase II-dependent chromatid core separation step in the formation of metaphase chromosomes. *J. Cell Biol.* 131:7–17. https://doi.org/10.1083/jcb.131.1.7

Gruber, S., C.H. Haering, and K. Nasmyth. 2003. Chromosomal cohesin forms a ring. *Cell.* 112:765–777. https://doi.org/10.1016/S0092-8674(03)00162-4

Guacci, V., D. Koshland, and A. Strunnikov. 1997. A direct link between sister chromatid cohesion and chromosome condensation revealed through the analysis of MCD1 in S. cerevisiae. *Cell.* 91:47–57. https://doi.org/10.1016/S0092-8674(01)80008-8

Guelen, L., L. Pagie, E. Brasset, W. Meuleman, M.B. Faza, W. Talhout, B.H. Eussen, A. de Klein, L. Wessels, W. de Laat, and B. van Steensel. 2008. Domain organization of human chromosomes revealed by mapping of nuclear lamina interactions. *Nature.* 453:948–951. https://doi.org/10.1038/nature06947

Haering, C.H., A.-M. Farcas, P. Arumugam, J. Metson, and K. Nasmyth. 2008. The cohesin ring concatenates sister DNA molecules. *Nature.* 454:297–301. https://doi.org/10.1038/nature07098

Hansen, A.S., I. Pustova, C. Cattoglio, R. Tjian, and X. Darzacq. 2017. CTCF and cohesin regulate chromatin loop stability with distinct dynamics. *eLife*. 6:2848. https://doi.org/10.7554/eLife.25776

Hansen, R.S., S. Thomas, R. Sandstrom, T.K. Canfield, R.E. Thurman, M. Weaver, M.O. Dorschner, S.M. Gartler, and J.A. Stamatoyannopoulos. 2010. Sequencing newly replicated DNA reveals widespread plasticity in human replication timing. *Proc. Natl. Acad. Sci. USA*. 107:139–144. https://doi.org/10.1073/pnas.0912402107

Held, M., M.H.A. Schmitz, B. Fischer, T. Walter, B. Neumann, M.H. Olma, M. Peter, J. Ellenberg, and D.W. Gerlich. 2010. CellCognition: time-resolved phenotype annotation in high-throughput live cell imaging. *Nat. Methods*. 7:747–754. https://doi.org/10.1038/nmeth.1486

Kagey, M.H., J.J. Newman, S. Bilodeau, Y. Zhan, D.A. Orlando, N.L. van Berkum, C.C. Ebmeier, J. Goossens, P.B. Rahl, S.S. Levine, et al. 2010. Mediator and cohesin connect gene expression and chromatin architecture. *Nature*. 467:430–435. https://doi.org/10.1038/nature09380

Khokhlov, A.R., and A.Y. Grosberg. 1994. Statistical Physics of Macromolecules. Springer. New York.

Kireeva, N., M. Lakonishok, I. Kireev, T. Hirano, and A.S. Belmont. 2004. Visualization of early chromosome condensation: a hierarchical folding, axial glue model of chromosome structure. *J. Cell Biol.* 166:775–785. https://doi.org/10.1083/jcb.200406049

Kueng, S., B. Hegemann, B.H. Peters, J.J. Lipp, A. Schleiffer, K. Mechtler, and J.-M. Peters. 2006. Wapl controls the dynamic association of cohesin with chromatin. *Cell*. 127:955–967. https://doi.org/10.1016/j.cell.2006.09.040

Ladurner, R., E. Kreidl, M.P. Ivanov, H. Ekker, M.H. Idarraga-Amado, G.A. Busslinger, G. Wutz, D.A. Cisneros, and J.-M. Peters. 2016. Sororin actively maintains sister chromatid cohesion. *EMBO J.* 35:635–653. https://doi.org/10.15252/embj.201592532

Landry, J.J.M., P.T. Pyl, T. Rausch, T. Zichner, M.M. Tekkedil, A.M. Stütz, A. Jauch, R.S. Aiyar, G. Pau, N. Delhomme, et al. 2013. The genomic and transcriptomic landscape of a HeLa cell line. *G3 (Bethesda)*. 3:1213–1224. https://doi.org/10.1534/g3.113.005777

Lengronne, A., Y. Katou, S. Mori, S. Yokobayashi, G.P. Kelly, T. Itoh, Y. Watanabe, K. Shirahige, and F. Uhlmann. 2004. Cohesin relocation from sites of chromosomal loading to places of convergent transcription. *Nature*. 430:573–578. https://doi.org/10.1038/nature02742

Leonhardt, H., H.P. Rahn, P. Weinzierl, A. Sporbert, T. Cremer, D. Zink, and M.C. Cardoso. 2000. Dynamics of DNA replication factories in living cells. *J. Cell Biol.* 149:271–280. https://doi.org/10.1083/jcb.149.2.271

Liang, Z., D. Zickler, M. Prentiss, F.S. Chang, G. Witz, K. Maeshima, and N. Kleckner. 2015. Chromosomes Progress to Metaphase in Multiple Discrete Steps via Global Compaction/Expansion Cycles. *Cell*. 161:1124–1137. https://doi.org/10.1016/j.cell.2015.04.030

Lucas, J.S., Y. Zhang, O.K. Dudko, and C. Murre. 2014. 3D trajectories adopted by coding and regulatory DNA elements: first-passage times for genomic interactions. *Cell*. 158:339–352. https://doi.org/10.1016/j.cell.2014.05.036

Lukinavičius, G., C. Blaukopf, E. Pershagen, A. Schena, L. Reymond, E. Derivery, M. González-Gaitán, E. D'Este, S.W. Hell, D.W. Gerlich, and K. Johnsson. 2015. SiR-Hoechst is a far-red DNA stain for live-cell nanoscopy. *Nat. Commun.* 6:8497. https://doi.org/10.1038/ncomms9497

Michaelis, C., R. Ciosk, and K. Nasmyth. 1997. Cohesins: chromosomal proteins that prevent premature separation of sister chromatids. *Cell*. 91:35–45. https://doi.org/10.1016/S0092-8674(01)80007-6

Mlynarczyk-Evans, S., M. Royce-Tolland, M.K. Alexander, A.A. Andersen, S. Kalantry, J. Gribnau, and B. Panning. 2006. X chromosomes alternate between two states prior to random X-inactivation. *PLoS Biol.* 4:e159. https://doi.org/10.1371/journal.pbio.0040159

Nagasaka, K., M.J. Hossain, M.J. Roberti, J. Ellenberg, and T. Hirota. 2016. Sister chromatid resolution is an intrinsic part of chromosome organization in prophase. *Nat. Cell Biol.* 18:692–699. https://doi.org/10.1038/ncb3353

Nasmyth, K. 2001. Disseminating the genome: joining, resolving, and separating sister chromatids during mitosis and meiosis. *Annu. Rev. Genet.* 35:673–745. https://doi.org/10.1146/annurev.genet.35.102401.091334

Nasmyth, K., and C.H. Haering. 2009. Cohesin: its roles and mechanisms. *Annu. Rev. Genet.* 43:525–558. https://doi.org/10.1146/annurev-genet-102108-134233

Nishiyama, T., R. Ladurner, J. Schmitz, E. Kreidl, A. Schleiffer, V. Bhaskara, M. Bando, K. Shirahige, A.A. Hyman, K. Mechtler, and J.-M. Peters. 2010. Sororin mediates sister chromatid cohesion by antagonizing Wapl. *Cell*. 143:737–749. https://doi.org/10.1016/j.cell.2010.10.031

Nora, E.P., B.R. Lajoie, E.G. Schulz, L. Giorgetti, I. Okamoto, N. Servant, T. Piolot, N.L. van Berkum, J. Meisig, J. Sedat, et al. 2012. Spatial partitioning of the regulatory landscape of the X-inactivation centre. *Nature*. 485:381–385. https://doi.org/10.1038/nature11049

Pueschel, R., F. Coraggio, and P. Meister. 2016. From single genes to entire genomes: the search for a function of nuclear organization. *Development*. 143:910–923. https://doi.org/10.1242/dev.129007

Rankin, S., N.G. Ayad, and M.W. Kirschner. 2005. Sororin, a substrate of the anaphase-promoting complex, is required for sister chromatid cohesion in vertebrates. *Mol. Cell*. 18:185–200. https://doi.org/10.1016/j.molcel.2005.03.017

Rao, S.S.P., M.H. Huntley, N.C. Durand, E.K. Stamenova, I.D. Bochkov, J.T. Robinson, A.L. Sanborn, I. Machol, A.D. Omer, E.S. Lander, and E.L. Aiden. 2014. A 3D map of the human genome at kilobase resolution reveals principles of chromatin looping. *Cell*. 159:1665–1680. https://doi.org/10.1016/j.cell.2014.11.021

Rao, S.S.P., S.-C. Huang, B. Glenn St Hilaire, J.M. Engreitz, E.M. Perez, K.-R. Kieffer-Kwon, A.L. Sanborn, S.E. Johnstone, G.D. Bascom, I.D. Bochkov, et al. 2017. Cohesin Loss Eliminates All Loop Domains. *Cell*. 171:305–320. https://doi.org/10.1016/j.cell.2017.09.026

Rhodes, J.D.P., J.H.I. Haarhuis, J.B. Grimm, B.D. Rowland, L.D. Lavis, and K.A. Nasmyth. 2017. Cohesin Can Remain Associated with Chromosomes during DNA Replication. *Cell Reports*. 20:2749–2755. https://doi.org/10.1016/j.celrep.2017.08.092

Robinson, J.T., H. Thorvaldsdóttir, W. Winckler, M. Guttman, E.S. Lander, G. Getz, and J.P. Mesirov. 2011. Integrative genomics viewer. *Nat. Biotechnol.* 29:24–26. https://doi.org/10.1038/nbt.1754

Samwer, M., M.W.G. Schneider, R. Hoefler, P.S. Schmalhorst, J.G. Jude, J. Zuber, and D.W. Gerlich. 2017. DNA Cross-Bridging Shapes a Single Nucleus from a Set of Mitotic Chromosomes. *Cell*. 170:956–972. https://doi.org/10.1016/j.cell.2017.07.038

Sanborn, A.L., S.S.P. Rao, S.-C. Huang, N.C. Durand, M.H. Huntley, A.I. Jewett, I.D. Bochkov, D. Chinnappan, A. Cutkosky, J. Li, et al. 2015. Chromatin extrusion explains key features of loop and domain formation in wild-type and engineered genomes. *Proc. Natl. Acad. Sci. USA*. 112:E6456–E6465. https://doi.org/10.1073/pnas.1518552112

Schindelin, J., I. Arganda-Carreras, E. Frise, V. Kaynig, M. Longair, T. Pietzsch, S. Preibisch, C. Rueden, S. Saalfeld, B. Schmid, et al. 2012. Fiji: an open-source platform for biological-image analysis. *Nat. Methods*. 9:676–682. https://doi.org/10.1038/nmeth.2019

Schmitz, J., E. Watrin, P. Lénárt, K. Mechtler, and J.-M. Peters. 2007. Sororin is required for stable binding of cohesin to chromatin and for sister chromatid cohesion in interphase. *Curr. Biol.* 17:630–636. https://doi.org/10.1016/j.cub.2007.02.029

Schmitz, M.H.A., M. Held, V. Janssens, J.R.A. Hutchins, O. Hudecz, E. Ivanova, J. Goris, L. Trinkle-Mulcahy, A.I. Lamond, I. Poser, et al. 2010. Live-cell imaging RNAi screen identifies PP2A-B55alpha and importin-beta1 as key mitotic exit regulators in human cells. *Nat. Cell Biol.* 12:886–893. https://doi.org/10.1038/ncb2092

Schneider, V.A., T. Graves-Lindsay, K. Howe, N. Bouk, H.-C. Chen, P.A. Kitts, T.D. Murphy, K.D. Pruitt, F. Thibaud-Nissen, D. Albracht, et al. 2017. Evaluation of GRCh38 and de novo haploid genome assemblies demonstrates the enduring quality of the reference assembly. *Genome Res.* 27:849–864. https://doi.org/10.1101/gr.213611.116

Schwarzer, W., N. Abdennur, A. Goloborodko, A. Pekowska, G. Fudenberg, Y. Loe-Mie, N.A. Fonseca, W. Huber, C. Haering, L. Mirny, and F. Spitz. 2016. Two independent modes of chromosome organization are revealed by cohesin removal. *bioRxiv*. https://doi.org/10.1101/094185

Selig, S., K. Okumura, D.C. Ward, and H. Cedar. 1992. Delineation of DNA replication time zones by fluorescence in situ hybridization. *EMBO J.* 11:1217–1225.

Shalem, O., N.E. Sanjana, E. Hartenian, X. Shi, D.A. Scott, T. Mikkelson, D. Heckl, B.L. Ebert, D.E. Root, J.G. Doench, and F. Zhang. 2014. Genome-scale CRISPR-Cas9 knockout screening in human cells. *Science*. 343:84–87. https://doi.org/10.1126/science.1247005

Stigler, J., G.Ö. Çamdere, D.E. Koshland, and E.C. Greene. 2016. Single-Molecule Imaging Reveals a Collapsed Conformational State for DNA-Bound Cohesin. *Cell Reports*. 15:988–998. https://doi.org/10.1016/j.celrep.2016.04.003

Tanenbaum, M.E., L.A. Gilbert, L.S. Qi, J.S. Weissman, and R.D. Vale. 2014. A protein-tagging system for signal amplification in gene expression and fluorescence imaging. *Cell*. 159:635–646. https://doi.org/10.1016/j.cell.2014.09.039

VanDerWal, J., Falconi, L., Januchowski, S., Shoo, L. P. & Storlie, C. SDMTools: Species distribution modelling tools: Tools for processing data associated with species distribution modelling exercises. R package version 1.1-6 (2011).

Volpi, E.V., D. Sheer, and F. Uhlmann. 2001. Cohesion, but not too close. *Curr. Biol.* 11:R378. https://doi.org/10.1016/S0960-9822(01)00212-3

Wutz, G., C. Várnai, K. Nagasaka, D.A. Cisneros, R.R. Stocsits, W. Tang, S. Schoenfelder, G. Jessberger, M. Muhar, M.J. Hossain, et al. 2017. Topologically associating domains and chromatin loops depend on cohesin and are regulated by CTCF, WAPL, and PDS5 proteins. *EMBO J.* 36:3573–3599. https://doi.org/10.15252/embj.201798004

Zhang, Y., T. Liu, C.A. Meyer, J. Eeckhoute, D.S. Johnson, B.E. Bernstein, C. Nusbaum, R.M. Myers, M. Brown, W. Li, et al. 2008. Model-based Analysis of ChIP-Seq (MACS). *Genome Biol.* 9:R137.

Zuin, J., J.R. Dixon, M.I.J.A. van der Reijden, Z. Ye, P. Kolovos, R.W.W. Brouwer, M.P.C. van de Corput, H.J.G. van de Werken, T.A. Knoch, W.F.J. van IJcken, et al. 2014a. Cohesin and CTCF differentially affect chromatin architecture and gene expression in human cells. *Proc. Natl. Acad. Sci. USA.* 111:996–1001. https://doi.org/10.1073/pnas.1317788111

Zuin, J., V. Franke, W.F.J. van Ijcken, A. van der Sloot, I.D. Krantz, M.I.J.A. van der Reijden, R. Nakato, B. Lenhard, and K.S. Wendt. 2014b. A cohesin-independent role for NIPBL at promoters provides insights in CdLS. *PLoS Genet.* 10:e1004153. https://doi.org/10.1371/journal.pgen.1004153